

Three-dimensional hydrodynamical CO⁵BOLD model atmospheres of red giant stars

II. Spectral line formation in the atmosphere of a giant located near the RGB tip

A. Kučinskas^{1,2}, M. Steffen³, H.-G. Ludwig⁴, V. Dobrovolskas², A. Ivanauskas^{2,1}, J. Klevas¹, D. Prakashavičius¹, E. Caffau⁴, and P. Bonifacio⁵

¹ Vilnius University Institute of Theoretical Physics and Astronomy, A. Goštauto 12, Vilnius LT-01108, Lithuania
e-mail: arunas.kucinskas, augustinas.ivanaukas, jonas.klevas, dainius.prakashavičius@tfai.vu.lt

² Vilnius University Astronomical Observatory, M. K. Čiurlionio 29, Vilnius LT-03100, Lithuania
e-mail: Vidas.Dobrovolskas@ff.vu.lt

³ Leibniz-Institut für Astrophysik Potsdam, An der Sternwarte 16, D-14482 Potsdam, Germany
e-mail: msteffen@aip.de

⁴ ZAH Landessternwarte Königstuhl, D-69117 Heidelberg, Germany
e-mail: hludwig, elcaffau@lsw.uni-heidelberg.de

⁵ GEPI, Observatoire de Paris, CNRS, Université Paris Diderot, Place Jules Janssen, 92190 Meudon, France
e-mail: piercarlo.bonifacio@obspm.fr

Received: date; accepted: date

ABSTRACT

Aims. We investigate the role of convection in the formation of atomic and molecular lines in the atmosphere of a red giant star. For this purpose we study the formation properties of spectral lines that belong to a number of astrophysically important tracer elements, including neutral and singly ionized atoms (Li I, N I, O I, Na I, Mg I, Al I, Si I, Si II, S I, K I, Ca I, Ca II, Ti I, Ti II, Cr I, Cr II, Mn I, Fe I, Fe II, Co I, Ni I, Zn I, Sr II, Ba II, and Eu II), and molecules (CH, CO, C₂, NH, CN, and OH).

Methods. We focus our investigation on a prototypical red giant located close to the red giant branch (RGB) tip ($T_{\text{eff}}=3660$ K, $\log g=1.0$, $[M/H]=0.0$). We used two types of model atmospheres, 3D hydrodynamical and classical 1D, calculated with the CO⁵BOLD and LHD stellar atmosphere codes, respectively. Both codes share the same atmospheric parameters, chemical composition, equation of state, and opacities, which allowed us to make a strictly differential comparison between the line formation properties predicted in 3D and 1D. The influence of convection on the spectral line formation was assessed with the aid of 3D–1D abundance corrections, which measure the difference between the abundances of chemical species derived with the 3D hydrodynamical and 1D classical model atmospheres.

Results. We find that convection plays a significant role in the spectral line formation in this particular red giant. The derived 3D–1D abundance corrections rarely exceed ± 0.1 dex when lines of neutral atoms and molecules are considered, which is in line with the previous findings for solar-metallicity red giants located on the lower RGB. The situation is different with lines that belong to ionized atoms, or to neutral atoms with high ionization potential. In both cases, the corrections for high-excitation lines ($\chi > 8$ eV) may amount to $\Delta_{3D-1D} \sim -0.4$ dex. The 3D–1D abundance corrections generally show a significant wavelength dependence; in most cases they are smaller in the near-infrared, at 1600–2500 nm.

Key words. stars: atmospheres – stars: late-type – stars: abundances – line: formation – convection – hydrodynamics

1. Introduction

Current three-dimensional (3D) hydrodynamical codes have brought a new level of realism to the modeling of stellar atmospheres, making it possible to assess the influence of various nonstationary phenomena on the observable properties of various classes of stars. Since red giants are amongst the brightest objects in intermediate age and old populations, precise understanding of their internal structures and observable properties is of key importance for studies of stellar populations in the Galaxy and beyond. Three-dimensional hydrodynamical stellar model atmospheres may prove especially useful in this context, as they can provide important theoretical insights about how and

to which extent convection and other nonstationary phenomena may influence the observable properties of red giant stars.

Up to now, only a few studies have focused on the investigation of observable properties of red giants with 3D hydrodynamical stellar model atmospheres. In one of the early attempts, Kučinskas et al. (2005) have found that convection may noticeably alter the thermal structure of the red giant atmosphere which, in turn, may affect the spectral energy distribution of the emerging radiation field. This may yield a difference of $\sim 0.2 - 0.3$ mag in broad-band photometric colors predicted by the 3D hydrodynamical and classical 1D models. It was later shown by Collet et al. (2007) that convection in the atmospheres of somewhat warmer red giants ($T_{\text{eff}} \approx 4700 - 5100$ K, $\log g = 2.2$, $[Fe/H] = 0.0$ to -3.0) may lead to significant changes in their thermal structures, especially at lowest metallic-

ities. Remarkably, at $[M/H] = -3.0$ this may result in differences of up to -1.0 dex in the abundances of chemical elements derived with the 3D hydrodynamical and classical 1D model atmospheres. This result was later confirmed by Dobrovolskas et al. (2010) and Ivanauskas et al. (2010), who used different 3D hydrodynamical stellar atmosphere and spectrum synthesis codes, CO⁵BOLD and Linfor3D, respectively, together with the atmospheric parameters of red giants similar to those utilized by Collet et al. (2007). All these studies unequivocally point to the fact that the role of convection in the atmospheres of red giant stars may be significantly more important than previously thought, especially at metallicities $[M/H] \lesssim -1.0$.

Aiming at a more systematic study, we have recently started a project to investigate internal structures and spectral properties of red giants across the HR diagram with the aid of 3D hydrodynamical model atmospheres. For this purpose we used the 3D hydrodynamical stellar atmosphere code CO⁵BOLD to produce a grid of red giant model atmospheres, which are now available as part of the CIFIST grid of CO⁵BOLD 3D model atmospheres (Ludwig et al. 2009, the grid is constantly updated with new models). In the first study of this series (Ludwig & Kučinskas 2012) we investigated physical properties of convection in the atmosphere of a red giant located close to the red giant branch (RGB) tip ($T_{\text{eff}} \approx 3660$ K, $\log g = 1.0$, $[M/H] = 0$). In the present study we extend our work on the same red giant and focus on the influence of convection on the formation of various atomic and molecular lines. Our main goal is to make a detailed comparison between the line strengths predicted by the 3D hydrodynamical and classical 1D models, and discuss the consequences for stellar abundance studies. General properties of the spectral energy distribution and photometric colors of this particular red giant will be discussed in a companion paper (Kučinskas et al. 2012, in preparation).

The paper is organized as follows. The model atmospheres used in this work are described in Sect. 2, where we also outline the details of spectrum synthesis calculations and the concept of 3D abundance corrections. The main results are presented in Sect. 3, including a brief discussion of the basic properties of spectral line formation in the presence of convection, and the differences between the predictions of the 3D hydrodynamical and classical 1D models. The conclusions are presented in Sect. 4. A more detailed analysis of the abundance corrections derived in this work as well as additional background information is given in Appendices A, B, and C.

2. Stellar model atmospheres and spectral line synthesis

2.1. Model atmospheres

We used red giant model atmospheres calculated with the 3D hydrodynamical CO⁵BOLD and 1D stationary LHD model atmosphere codes. Both models were computed for the same atmospheric parameters ($T_{\text{eff}}=3660$ K, $\log g=1.0$, $[M/H]=0.0$) and elemental composition, and with the same equation of state and opacities; they also share the same numerical radiative transfer scheme. Additionally, we also used an average $\langle 3D \rangle$ model, which was produced by spatially averaging the 3D model structures at constant Rosseland optical depth. The $\langle 3D \rangle$ model does not contain explicit information about the horizontal fluctuations of thermodynamical and hydrodynamical quantities (e.g. temperature, pressure, velocity) that are present in the full 3D model atmosphere. Therefore, the comparison of the predictions of the full 3D and average $\langle 3D \rangle$ models allows

one to estimate the relative importance of the horizontal temperature fluctuations on the spectral line formation (see, e.g. Caffau et al. 2011, for a more detailed discussion). Since the three types of models used in this work are described in detail by Ludwig & Kučinskas (2012), we only briefly summarize the most essential aspects of their calculation in the following subsections.

2.1.1. Three-dimensional hydrodynamical model and 3D snapshot selection

The red giant model atmosphere used in this work was calculated with the 3D radiation hydrodynamics code CO⁵BOLD (Freytag et al. 2012). The CO⁵BOLD code uses a Riemann solver of Roe type to calculate the time evolution of the hydrodynamical flow and the radiation field on a 3D Cartesian grid. The model was computed using a grid of $150 \times 150 \times 151$ mesh points ($x \times y \times z$), which corresponds to a physical box size of $15.6 \times 15.6 \times 8.6 \text{ Gm}^3$. The radiative transfer is based on monochromatic opacities from the MARCS stellar atmosphere package (Gustafsson et al. 2008) which, to speed up the calculations, were grouped into five opacity bins (for details on the opacity binning approach see, e.g. Nordlund 1982; Ludwig 1992; Ludwig et al. 1994; Vögler 2004). Solar elemental abundances as given by Grevesse & Sauval (1998) were assumed, except for carbon, nitrogen, and oxygen, for which the following values were used: $A(C)=8.41$, $A(N)=7.8$, and $A(O)=8.67$ (Caffau et al. 2008). The model calculations were made assuming local thermodynamic equilibrium, LTE (for more details about the model setup see Ludwig & Kučinskas 2012).

After the initial relaxation to a quasi-stationary state, we ran the model simulations to cover a span of $\sim 6 \times 10^6$ sec (~ 70 days) in stellar time. This corresponds to approximately seven convective turnover times¹ in the atmosphere of this particular red giant. From this sequence of relaxed models we selected 14 3D model structures computed at different instances in time (snapshots). Individual snapshots of this 14-snapshot subset were then used to produce average $\langle 3D \rangle$ model and spectrum synthesis calculations (Sect. 2.1.2 and 2.2, respectively). Snapshots of this 14-snapshot ensemble are separated by 5×10^5 sec (~ 6 days) in stellar time, which allows one to assume that in this subset they are statistically uncorrelated. The snapshots were selected in such a way that most important statistical properties of the snapshot ensemble, such as the average effective temperature and its standard deviation, mean velocity at optical depth unity, mean velocity profile and residual mass flux profile, would match those of the entire 3D model run as closely as possible.

2.1.2. Average $\langle 3D \rangle$ model

For each of the selected snapshots, the corresponding average 3D model, $\langle 3D \rangle$, was obtained by spatially averaging the thermal structure of the 3D model box on surfaces of equal Rosseland optical depth. We averaged the fourth moment of temperature and first moment of gas pressure to preserve the radiative properties of the original 3D model, according to the prescription given in Steffen et al. (1995). The product of this procedure is a 1D model atmosphere that retains the averaged vertical profile of the thermodynamical structure of the 3D model, but lacks explicit information about the horizontal inhomogeneities. This

¹ as measured by the Brunt-Vaisälä and/or advection timescales, the latter equal to the time needed for the convective material to cross 1.8 pressure scale heights (see Ludwig & Kučinskas 2012).

was done for the 14 3D model snapshots selected at different instants in time (Sect. 2.1.1), thus obtaining a sequence of 14 ⟨3D⟩ models.

2.1.3. One-dimensional (1D) model

The 1D hydrostatic model was calculated with the LHD code, using the same atmospheric parameters, elemental abundances, opacities, and equation of state as in the 3D model calculations described above (see, e.g., Caffau et al. 2008, for more details on the LHD code). Convection in the LHD models was treated according to the Mihalas (1978) formulation of the mixing-length theory. The LHD models were calculated for the mixing-length parameters $\alpha_{\text{MLT}} = 1.0$ and 2.0 , to investigate the influence of α_{MLT} on the properties of line formation in the 1D models (see Sect. 3.6).

2.2. Three- and one-dimensional spectrum synthesis calculations

2.2.1. Chemical elements and spectral line parameters

We used fictitious spectral lines, i.e., lines of a particular chemical element (molecule) for which the central wavelength, λ_c , the excitation potential of the lower level, χ , and line equivalent width, W , were selected arbitrarily. This approach allowed us to cover a range in λ_c and χ to quantify the trends of line formation properties in the 3D hydrodynamical and 1D classical model atmospheres with respect to these two line parameters. Conceptually, this method can be traced back to the work of Steffen & Holweger (2002) and was applied in several later studies too (e.g., Collet et al. 2007; Dobrovolskas et al. 2010; Ivanauskas et al. 2010).

Synthetic line profiles were calculated for the following tracer species of astrophysical interest:

- neutral atoms: Li I, N I, O I, Na I, Mg I, Al I, Si I, S I, K I, Ca I, Ti I, Cr I, Mn I, Fe I, Co I, Ni I, and Zn I;
- ionized atoms: Si II, Ca II, Ti II, Cr II, Fe II, Sr II, Ba II, and Eu II;
- molecules: CH, CO, C₂, NH, CN, and OH.

Fictitious lines were calculated at three wavelengths, $\lambda_c = 400, 850$, and 1600 nm. The first two were selected to bracket the wavelength range accessible with modern high-resolution optical spectrographs (e.g., UVES/GIRAFFE@VLT, HARPS@ESO3.6m, HIRES@Keck), whereas the third corresponds to the wavelength reachable with similar instruments in the near-infrared *H*-band (e.g., CRIRES@VLT, NIRSPEC@Keck). In the case of molecules, however, we used the wavelengths of real molecular bands in the blue part of the spectrum, whenever available: the A–X OH transition at 315 nm (e.g., Bessell et al. 2004), the A–X transition of NH at 336 nm (e.g., Spite et al. 2005), the B–X transition of CN at 388 nm (Lambert 1968), and the A–X electronic transition of CH at 432 nm (Gratton 1985). The exceptions were C₂ and C, which do not have bands in the UV, and for which we thus used the 400 nm reference wavelength instead. One should also note that 850 and 1600 nm coincide respectively with the maximum and minimum absorption of the H⁺ ion, which is the most important contributor to the continuum opacity in red giant atmospheres in the optical to near-infrared wavelength range. On the other hand, the continuum opacity at 400 nm is dominated by the contribution from metals. Therefore, the choice of the three wavelengths

offers a possibility to study the interplay between the different sources of continuum opacity and line formation.

The excitation potentials were selected to cover the range of χ combinations possible for real (i.e., nonfictitious) elements/lines. We used $\chi = 0–6$ eV for the neutral atoms, $0–10$ eV for the ions (in both cases with a step of $\Delta\chi = 2$ eV), and $0–4$ eV ($\Delta\chi = 1$ eV) for the molecules. Exceptions were O I and N I: their real lines are characterized by very high excitation potentials ($\chi > 9$ eV) and thus the χ range for these two species was chosen to be identical to that of the ions.

We finally stress that some of the elements/species studied here have only a few real lines that can be used in the spectroscopic diagnostics of red giant stars (e.g., Li I, N I, O I, S I). Moreover, we also included several elements whose spectral lines are inaccessible for observations in real life (e.g., K II, S II). We stress that all these elements were included to help understand the trends and properties of spectral line formation in the presence of realistically modeled convection, and to identify the physical causes behind them. Obviously, the exact values of abundance corrections for the combinations of atomic parameters where spectral lines of these elements do not exist (or may not be observed in stellar spectra) can only be of academical interest.

2.2.2. Spectral line synthesis with 3D, ⟨3D⟩, and 1D model atmospheres

Three-dimensional spectrum synthesis calculations are very time-consuming and thus performing them by using the entire 3D model sequence would be impractical. To make the task manageable, synthetic spectral line profiles were computed using 14 3D model structures (snapshots) selected from the sequence of seventy 3D models, fully relaxed to a quasi-stationary state (see Sect. 2.1.1). To speed-up calculations further, spectral synthesis was carried out on a coarser x, y grid of 50×50 points, i.e. using only one third of the grid points of the original 3D model box in each horizontal direction. Full-resolution test calculations performed on the original 150×150 grid show that the reduced horizontal resolution has a negligible effect on the properties of synthesized spectral lines.

For all elements investigated here, spectral line profiles corresponding to the 3D hydrodynamical model were calculated for each individual 3D model structure (snapshot) in the 14-snapshot ensemble. A composite 3D line profile was then constructed by co-adding the line profiles corresponding to all fourteen snapshots. Similarly, ⟨3D⟩ line profiles were calculated using a sequence of ⟨3D⟩ models obtained according to the prescription given in Sect. 2.1.2. Spectral line profiles were calculated for each of the fourteen ⟨3D⟩ models and then co-added to produce a composite ⟨3D⟩ line profile. A microturbulence velocity of $\xi_{\text{mic}} = 2.0$ km/s was used in the line synthesis calculations with ⟨3D⟩ and 1D models. The choice of ξ_{mic} is not critical since we used only weak unsaturated lines in the following (Sect. 2.3).

To enable a strictly differential comparison between the predictions of the 3D and 1D models, 3D, ⟨3D⟩, and 1D spectrum synthesis computations were made with the same spectrum synthesis code, Linfor3D². Additionally, as we stated above, the 3D and 1D models used in the computations shared identical atmospheric parameters, chemical composition, equation of state, and opacities. We therefore tried to minimize the differences in the model calculation procedure and line synthesis computations, so that any discrepancy in the predictions obtained with

² http://www.aip.de/~mst/Linfor3D/linfor_3D_manual.pdf

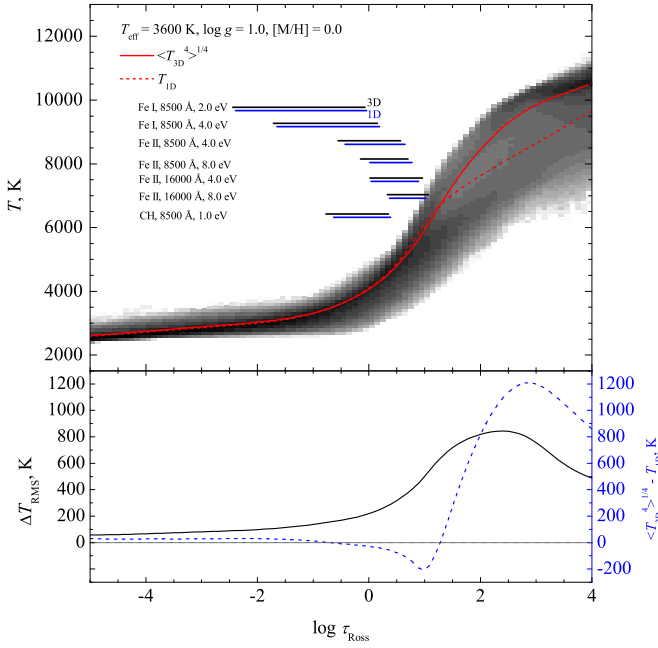


Fig. 1. Top panel: temperature profiles in the three model atmospheres of a red giant: 3D hydrodynamical (gray scales showing the logarithmic probability density of the 14-snapshot ensemble), average $\langle 3D \rangle$ (red solid line, average over the 14-snapshot ensemble), and 1D LHD model atmosphere with $\alpha_{MLT}=1.0$ (red dashed line). Horizontal bars indicate approximate formation regions of Fe I, Fe II, and CH lines in the 3D and 1D models, at different wavelengths and line excitation potentials (bars mark the regions where 90% of line equivalent width is acquired, i.e., between 5% and 95% in the cumulative line depression contribution function, see Appendix B). Bottom panel: RMS horizontal temperature fluctuations at constant τ_{Ross} in the 3D model (black solid line, 14-snapshot ensemble); and the difference between the temperature profiles corresponding to the average $\langle 3D \rangle$ (14-snapshot ensemble average) and the 1D model (blue dashed line).

3D and 1D models could be traced back to the differences in physical realism invoked in the two types of models.

2.3. 3D–1D abundance corrections

The influence of convection on the spectral line formation and the resulting line strengths was investigated with the aid of 3D–1D abundance corrections. The 3D–1D abundance correction, Δ_{3D-1D} , was defined as the difference in the abundance $A(X_i)$ of the element X_i obtained for a given equivalent width of a particular spectral line with the 3D hydrodynamical and classical 1D model atmospheres, $\Delta_{3D-1D} = A(X_i)_{3D} - A(X_i)_{1D}$ (see, e.g., Caffau et al. 2011). The contribution to the 3D–1D abundance correction comes from two major constituents: (a) the correction due to the horizontal temperature fluctuations in the 3D model, $\Delta_{3D-(3D)} = A(X_i)_{3D} - A(X_i)_{\langle 3D \rangle}$, and (b) the correction due to differences between the temperature profiles of the average $\langle 3D \rangle$ and 1D models, $\Delta_{\langle 3D \rangle-1D} = A(X_i)_{\langle 3D \rangle} - A(X_i)_{1D}$. The full abundance correction is a sum of the two constituents, $\Delta_{3D-1D} = \Delta_{3D-(3D)} + \Delta_{\langle 3D \rangle-1D}$.

The 3D–1D abundance corrections were always calculated for weak lines (equivalent width < 0.5 pm). The reason for this choice was that these weak lines are supposed to be on the linear

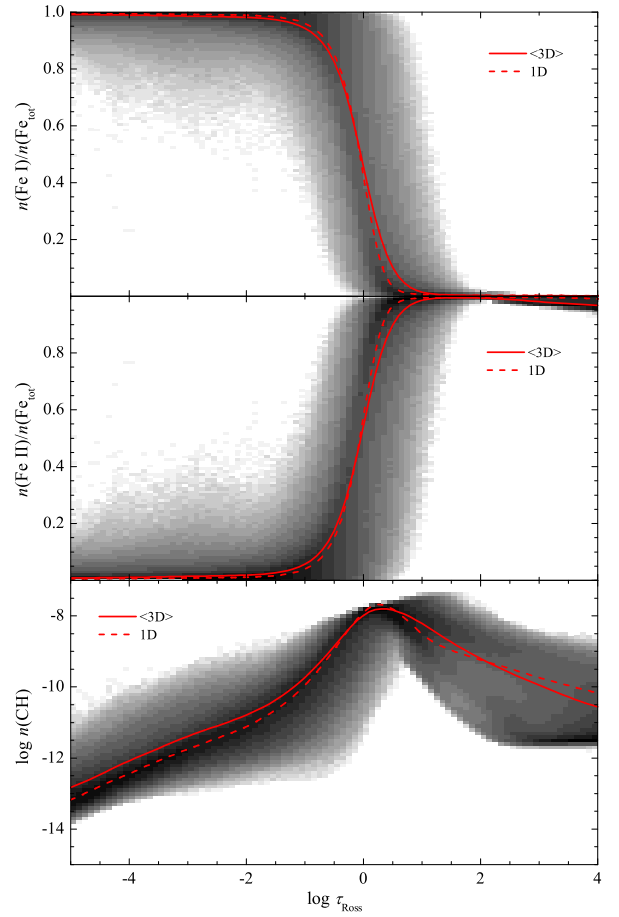


Fig. 2. Number densities of Fe I, Fe II, and CH (top-down), plotted versus τ_{Ross} for the three model atmospheres of a red giant: 3D hydrodynamical (gray scales showing the logarithmic probability density of the 14-snapshot ensemble), average $\langle 3D \rangle$ (solid line, 14-snapshot ensemble average), and 1D LHD model with $\alpha_{MLT}=1.0$ (dashed line). The number densities of Fe I and Fe II are provided as fractions of the total iron number density, $n(Fe_{tot})$, whereas that of CH is given on a scale where $n(H_{tot}) = 12.0$.

part of the curve-of-growth, where their equivalent width is independent of the microturbulence velocity, ξ_{mic} , used with the $\langle 3D \rangle$ and 1D models. Hence, the derived 3D–1D abundance corrections become independent of the choice of the microturbulence parameter.

3. Results and discussion

3.1. General properties of spectral line formation in the red giant atmosphere

Convection indeed plays an important role in shaping the upper atmosphere of the red giant studied here: convective up-flows and down-drafts dominate close to the optical surface (optical depth $\tau_{Ross} \approx 1$), whereas the shock-wave activity is most prominent in the outer atmosphere (see Ludwig & Kučinskas 2012). This alters the thermal structure of the atmosphere, in particular, by causing spatial and temporal variations of the temperature profiles in the 3D model (Fig. 1). Since local temperature sets the physical conditions for spectral line formation, it is reason-

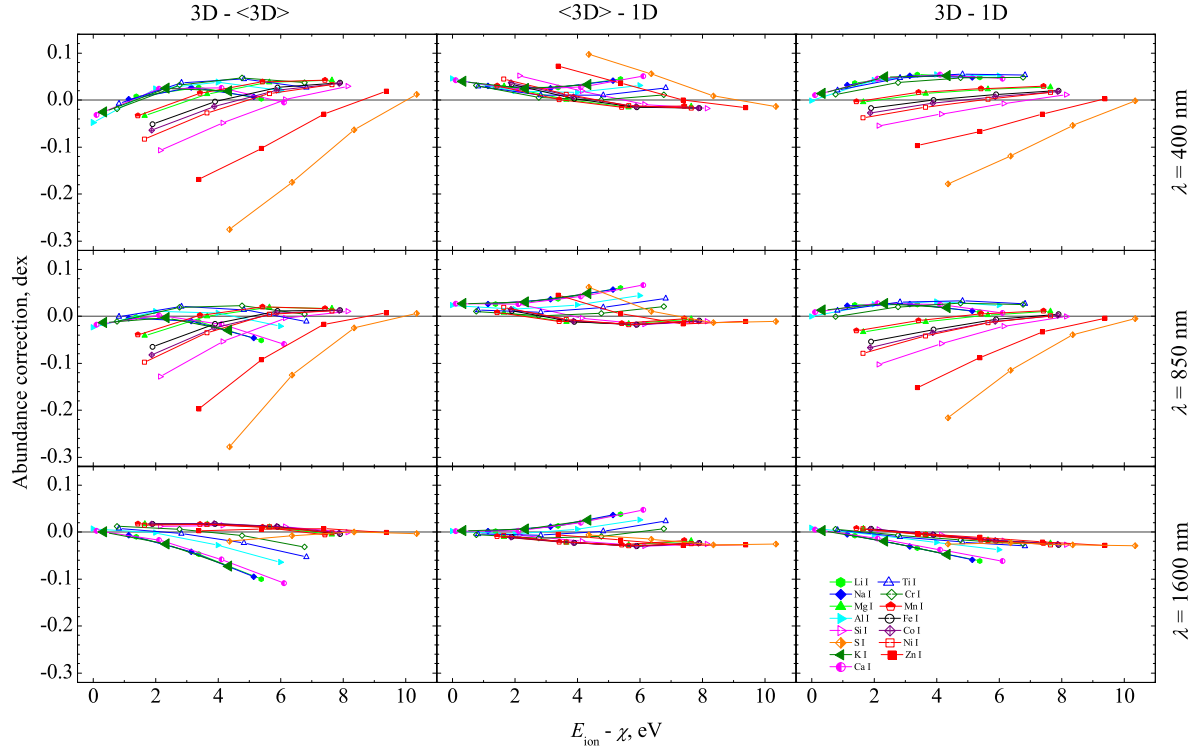


Fig. 3. Abundance corrections for spectral lines of neutral atoms, plotted versus the difference between their ionization energy and line excitation potential, $E_{\text{ion}} - \chi$. Three types of abundance corrections are shown: $\Delta_{3\text{D}-\langle 3\text{D} \rangle}$ (left column), $\Delta_{\langle 3\text{D} \rangle-1\text{D}}$ (middle column), and $\Delta_{3\text{D}-1\text{D}}$ (right column). Abundance corrections are provided at three different wavelengths: 400 nm (top row), 850 nm (middle row), and 1600 nm (bottom row). The ionization energies of neutral atoms used in plotting this figure are provided in Table 1.

able to expect that line profiles predicted by the 3D, $\langle 3\text{D} \rangle$, and 1D models will also be different.

Obviously, there are significant differences between the number densities of chemical species predicted by the 3D hydrodynamical and classical 1D models (Fig. 2). To a large extent, this behavior is defined by the atomic/molecular properties of individual species, such as ionization and dissociation potentials in case of atoms and molecules, respectively. This leads to different sensitivities of the number densities to temperature fluctuations. For example, species that are in the minority ionization stage at a given depth in the atmosphere (e.g., Fe II at $\log \tau_{\text{Ross}} \lesssim -0.2$) are very sensitive to temperature fluctuations, since small changes in the degree of ionization lead to a large spread in their number densities (as indicated by the width of the density plot in Fig. 2).

For a given set of spectral line parameters (such as wavelength, excitation potential, and oscillator strength), the line formation region is essentially defined by the temperature. Since differences between the temperature profiles of the average $\langle 3\text{D} \rangle$ and 1D models are small in the entire range of optical depths relevant to the line formation ($|\Delta T| \lesssim 200$ K in the range of $\log \tau_{\text{Ross}} \lesssim 1.0$, Fig. 1), this leads to very similar line formation spans in the $\langle 3\text{D} \rangle$ and 1D models. On the other hand, the presence of horizontal temperature fluctuations in the line forming layers plays a major role in the 3D line formation process, leading in general to line strengthening with respect to the $\langle 3\text{D} \rangle$ case. The amplitude of the deviations from the average $\langle 3\text{D} \rangle$ temperature profile, as defined by the RMS horizontal temperature fluctuations ($\Delta T_{\text{RMS}} = \sqrt{\langle (T - T_0)^2 \rangle_{x,y,t}}$, where $\langle \cdot \rangle_{x,y,t}$ denotes temporal and horizontal averaging on surfaces of equal optical depth, and $T_0 = \langle T \rangle_{x,y,t}$ is the depth-dependent average temperature), is monotonically decreasing throughout the entire photo-

Table 1. Ionization energies of various neutral atoms.

Element	E_{ion} , eV ^a	Element	E_{ion} , eV ^a	Element	E_{ion} , eV ^a
Li I	5.39	Si I	10.36	Mn I	7.43
Na I	5.14	K I	4.34	Fe I	7.90
Mg I	7.65	Ca I	6.11	Co I	7.88
Al I	5.99	Ti I	6.83	Ni I	7.64
Si I	8.15	Cr I	6.77	Zn I	9.39

^a NIST database, <https://www.nist.gov>

sphere, from 500 K at $\log \tau_{\text{Ross}} = +1.0$ to 50 K at $\log \tau_{\text{Ross}} = -5$ (Fig. 1). We thus expect the differences between 3D and $\langle 3\text{D} \rangle$ line formation to show up most clearly for high-excitation lines, forming in the deep photosphere where the horizontal temperature fluctuations are large. At the same time, the differences between the average $\langle 3\text{D} \rangle$ and 1D temperature profiles will also be most pronounced in this part of the atmosphere, such that the $\langle 3\text{D} \rangle$ –1D effects should also be strongest for the high-excitation lines.

3.2. Abundance corrections for lines of neutral atoms

The abundance corrections obtained for the bulk of neutral atoms are plotted in Fig. 3 versus the difference between their ionization and excitation potentials, $E_{\text{ion}} - \chi$. This choice of abscissa was motivated by the fact that for chemical elements that are almost completely ionized in the line-forming regions,

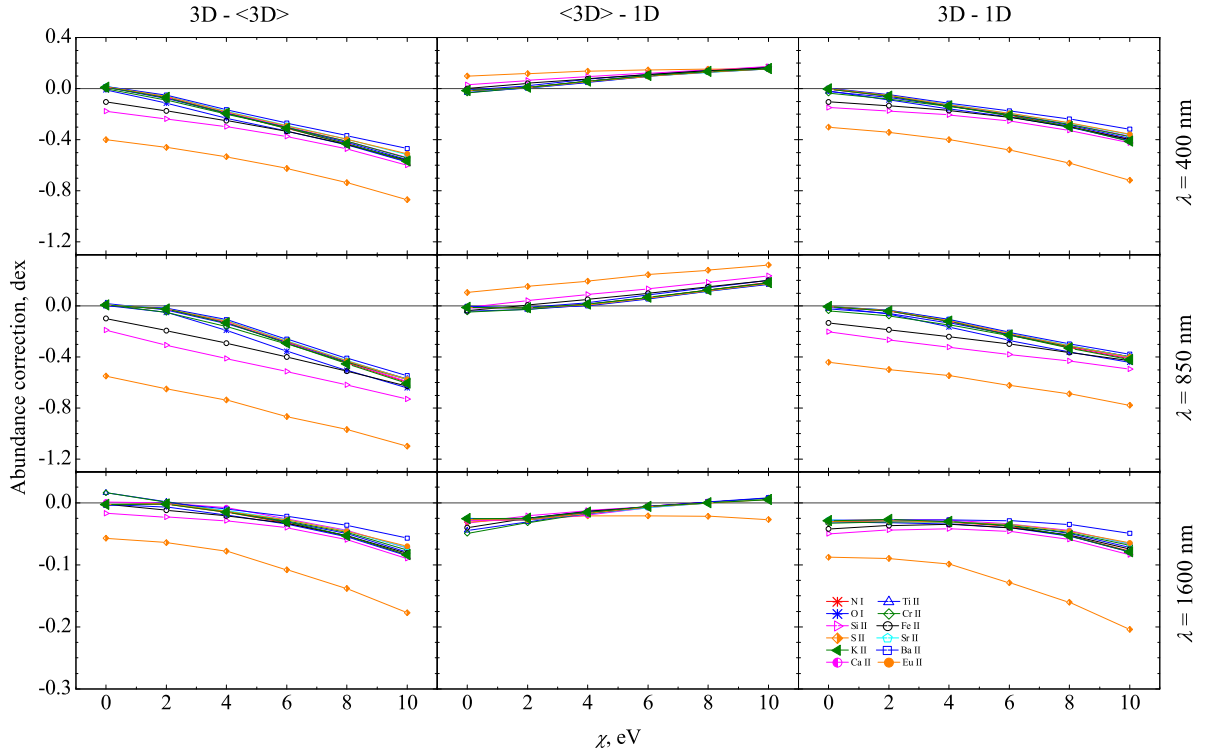


Fig. 4. Abundance corrections for spectral lines of ionized atoms (plus N I and O I), plotted versus the line excitation potential, χ (other notations as in Fig. 3).

it is the *difference* $E_{\text{ion}} - \chi$ (and of course the thermodynamical conditions) that defines the number density of the neutral atoms per unit mass. The line opacity of this minority species is thus proportional to the combined Saha-Boltzmann factor, $\kappa_\ell \sim \exp\{+(E_{\text{ion}} - \chi)/kT\}$ (cf. Gray 2005, in the analysis of the temperature dependence of the line strength). The abundance correction curves shown in Fig. 3 must therefore fall on top of each other for all neutral atoms of elements that are strongly ionized (i.e. those with sufficiently low ionization potential, $E_{\text{ion}} \lesssim 6$ eV), as explained in more detail in Appendix A. Indeed, this is clearly the case for the abundance corrections of Li I, Na I, and K I, which are in their minority ionization stage throughout the entire atmosphere of this particular red giant. For this type of atoms, the total abundance correction, $\Delta_{3\text{D}-1\text{D}}$, and its constituents, $\Delta_{3\text{D}-\langle 3\text{D} \rangle}$ and $\Delta_{\langle 3\text{D} \rangle-1\text{D}}$, are confined to the range of $-0.1 \dots +0.05$ dex, with comparable contributions (of different sign) from the $\Delta_{3\text{D}-\langle 3\text{D} \rangle}$ and $\Delta_{\langle 3\text{D} \rangle-1\text{D}}$ corrections. All corrections are more negative in the near-IR at λ 1600 nm than in the red at λ 850 nm.

For higher ionization potential, neutral atoms gradually turn into majority species, and the abundance correction curves in Fig. 3 begin to separate. The two type of lines behave radically different, and this can be clearly distinguished in the $\Delta_{3\text{D}-1\text{D}}$ versus $E_{\text{ion}} - \chi$ plot. This behavior is simply a consequence of the combined action of ionization and excitation, as demonstrated in Appendix A. The point is that the ionization factor dominates over the excitation factor as long as the neutral atoms are a *minority species*, and thus the line opacity decreases with increasing temperature; low-excitation lines are then most temperature-sensitive. The reverse is true for a neutral *majority species*. Here the excitation factor dominates over the ionization factor, and the line opacity increases with increasing temperature,

$\kappa_\ell \sim \exp\{-\chi/kT\}$ (cf. Gray 2005, Chapter 13, Case 1). In this situation, high-excitation lines are most temperature-sensitive.

The largest (most negative) 3D corrections are obtained for Zn I and S I, reaching down to $\Delta_{3\text{D}-\langle 3\text{D} \rangle} \approx -0.20$ and -0.28 dex, respectively. This is explained by the fact that these species have the highest ionization potentials of all atoms shown in Fig. 3: the high-excitation lines of these atoms have the most temperature-sensitive Boltzmann factor, and at the same time form in the deep photosphere where the temperature fluctuations are more pronounced than in the higher photospheric layers where the lines of the minority species originate. Surprisingly, the corrections for all atoms of majority type are much smaller at λ 1600 nm than at λ 850 nm (see Appendix B for a detailed explanation). We note that neutral atoms with the highest ionization potentials behave as the majority ions shown in Fig. 4, where N I ($E_{\text{ion}} = 14.53$ eV) and O I ($E_{\text{ion}} = 13.62$ eV) have already been included. The abundance corrections for the ions (and neutral majority species) show the same strong wavelength dependence. They are discussed in the next section.

3.3. Abundance corrections for lines of ionized atoms

Figure 4 displays the abundance corrections for a selection of ionized atoms (plus N I and O I), showing a rather uniform dependence on excitation potential χ . We first consider the ions that represent the majority ionization stage. Their line opacity (per unit mass) depends on temperature as $\kappa_\ell \sim \exp\{-\chi/kT\}$. Owing to its low first ionization potential, K II is present in its majority ionization stage throughout the entire atmosphere of this red giant (K II is only plotted for tracing the behavior of elements that are nearly 100% ionized; K II lines are inaccessible to observations in real red giant atmospheres). The majority neutral atoms N I and O I show exactly the same temperature sen-

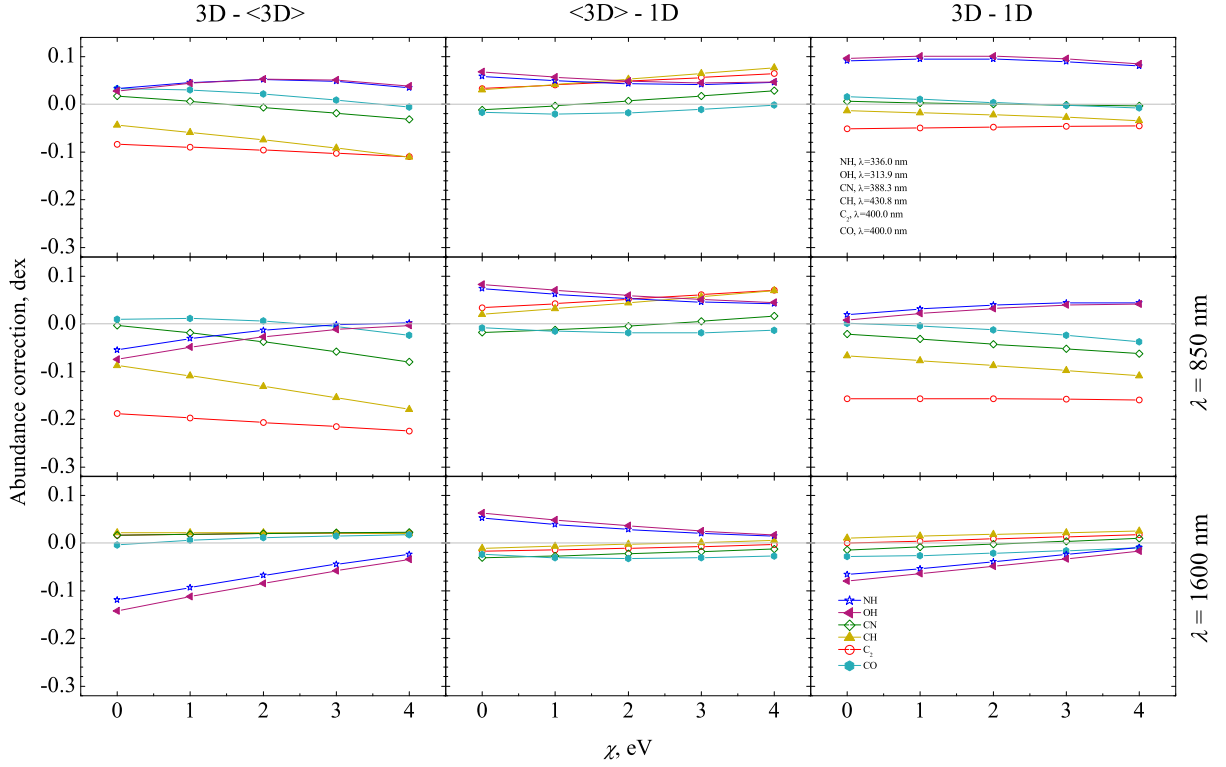


Fig. 5. Same as in Fig. 4 but for molecular lines. The bluest wavelength (top row) corresponds to the real wavelength of molecular bands in this spectral range (see legend), except for C₂ and CO, which do not have bands in the UV. The curve corresponding to C₂ coincides with that of CN in the lower left panel. Note the different y-scale in the lowest three panels.

sitivity (see Sect. 3.2), and hence their 3D–1D abundance corrections coincide with those of the majority ions. The corrections vanish for ground-state lines and increase steadily in amplitude toward the high-excitation lines. At $\chi = 10$ eV, $\Delta_{3D-(3D)}$ amounts to ≈ -0.6 dex, while $\Delta_{(3D)-1D}$ reaches $\approx +0.2$ dex, hence $\Delta_{3D-1D} \approx -0.4$ dex. For ions that are no pure majority species, the abundance corrections depend weakly on the ionization potential, systematically increasing in absolute size with E_{ion} .

Basically, the curves shown in Fig. 4 reflect the temperature sensitivity of the line opacity, which simply scales with the excitation potential, $\partial \log \kappa_\ell / \partial \log T = \chi / (kT)$ (valid for the majority species). All abundance corrections are therefore close to zero for $\chi = 0$, and increase systematically with χ . Since the $\langle 3D \rangle$ model is cooler in the line-forming regions than the 1D model, the same line is weaker in the $\langle 3D \rangle$ model than the 1D model, such that $\Delta_{(3D)-1D} \sim -\chi (\log T_{(3D)} - \log T_{1D})$ is positive. On the other hand, $\Delta_{3D-(3D)}$ is negative, because the horizontally averaged line opacity in the 3D model exceeds the line opacity obtained for the horizontally averaged temperature, $\langle \kappa_\ell \rangle > \kappa_\ell(\langle T \rangle) \approx \kappa_\ell(T_{(3D)})$, essentially because of the highly non-linear temperature dependence of κ_ℓ ($\partial^2 \kappa_\ell / \partial T^2 > 0$).

In this simple picture, the abundance corrections should be similar for all wavelengths, since the temperature sensitivity of the line opacity is wavelength independent (apart from a weak dependence through the stimulated emission factor). Obviously, this is not the case: the abundance corrections are much larger in the red at λ 850 nm than in the near-IR at λ 1600 nm, even though the near-IR lines form at deeper photospheric layers where the amplitude of the temperature fluctuations should be larger (Fig. 1, lower panel). A detailed explanation of this counter-intuitive behavior is given in Appendix B. In short, it is not the

line opacity alone that determines the strength of a spectral line, but rather the ratio of line-to-continuum opacity. It turns out that the continuum opacity at λ 850 nm (due to H[−] bound-free absorption) is almost independent of temperature, such that the T -dependence of the line opacity dominates the abundance corrections. At λ 1600 nm, however, the continuum opacity (due to H[−] free-free absorption) is strongly T -dependent, leading to a substantial reduction of the temperature sensitivity of the ratio κ_ℓ / κ_c , and hence to much smaller abundance corrections than at λ 850 nm.

Finally, we note that the S II line exhibits by far the largest abundance corrections, reaching $\Delta_{3D-(3D)} \approx -1.1$ dex at $\chi = 10$ eV. This outstanding behavior is related to the high ionization potential of S I ($E_{ion} = 10.36$ eV), making S II a true minority ion. In this case, the line opacity is proportional to $\exp\{-(E_{ion} + \chi)/kT\}$ (cf. Gray 2005, Chapter 13, Case 3). This extremely high temperature dependence gives rise to the extraordinary abundance corrections. In compliance with this interpretation, $\Delta_{3D-(3D)}$ for S II at $\chi = 0$ is already as large as $\Delta_{3D-(3D)}$ at $\chi = 10$ eV for the normal majority ions. We note, however, that this is probably a purely academic case, since such lines would certainly be too weak to be observable.

3.4. Abundance corrections for molecular lines

Figure 5 displays the abundance corrections for a selection of molecules as a function of the excitation potential χ . The total abundance corrections (right column) range from $\Delta_{3D-1D} \approx -0.16$ dex for C₂ at λ 850 nm to $\approx +0.1$ dex for NH and OH in the UV. As in the case of neutral atoms, the $\Delta_{3D-(3D)}$ and $\Delta_{(3D)-1D}$ corrections are often of opposite sign, making the total abun-

dance correction, Δ_{3D-1D} , slightly smaller than the granulation correction $\Delta_{3D-(3D)}$.

A detailed interpretation of the molecular abundance corrections is more complicated than in the case of neutral atoms and ions, because the dissociation equilibria of all molecules are closely coupled, such that their number densities are intimately related and in some cases show an unexpected temperature dependence. For basic orientation, Fig. C.1 (Appendix C) shows the depth-dependence of the molecule concentrations (number densities normalized to total number density of carbon nuclei) in the 1D LHD model.

First of all, because of its high dissociation energy of $D_0 = 11.1$ eV, CO is a majority species throughout the whole photosphere; practically all carbon nuclei are locked in this molecule at $\tau_{\text{Ross}} < 1$, whereas CO dissociates quickly in the deeper photosphere. In terms of abundance corrections, CO behaves like the majority species shown in Fig. 4. The dependence on excitation potential is weaker, however. Owing to dissociation in the deeper layers, the excited CO lines form higher up in the atmosphere than the majority ions with the same χ , and thus feel weaker temperature fluctuations and a reduced $\langle 3D \rangle$ –1D temperature difference. As a consequence, the 3D abundance corrections are small in the studied range of excitation potentials.

The molecules NH and OH belong to a different class of molecules. Their constituents (H, N, and O) are majority species but only a tiny fraction of N and O is bound in NH and OH molecules, respectively. In this situation, the molecular line opacity is proportional to the Boltzmann factor $\exp[(D_0 - \chi)/kT]$, i.e. it depends on the difference between dissociation energy D_0 and excitation potential χ . The largest abundance corrections are therefore found for $\chi = 0$, where the line opacity has the highest temperature sensitivity (see Appendix C, Eq. C.5). In fact, the abundance corrections of these molecular lines behave very much like those of the true minority neutral atoms shown in Fig. 3. This is also true for their wavelength dependence.

The molecules CN, CH, and C₂ fall in yet another category. Their temperature dependence is opposite to that of the other molecules, i.e. their number density increases toward higher temperature (at constant density or constant pressure). The reason is a strong coupling to the dissociation equilibrium of CO, which controls the number density of free carbon atoms. Higher temperatures lead to some dissociation of CO, hence an increased concentration of carbon atoms, and in turn to higher densities of CN, CH, and C₂. CH is more sensitive to this coupling than CN, because the latter has a higher dissociation energy. The C₂ molecule is most sensitive since its concentration depends on the square of the number density of free carbon atoms. The abundance corrections $\Delta_{3D-(3D)}$ at λ 850 nm are therefore largest (most negative) for C₂.

At λ 1600 nm, the fluctuation of the continuum opacity is stronger than in the red at λ 850 nm, because (i) the temperature fluctuations are larger in the deeper layers where the near-IR lines form, and (ii) the temperature dependence³ of the continuum opacity is stronger in the near-IR (see Fig. B.2). For molecules like NH and OH, the $3D$ – $\langle 3D \rangle$ corrections are larger (more negative) at λ 1600 nm since κ_ℓ decreases while κ_c increases with T , such that the fluctuations of the ratio κ_ℓ/κ_c are stronger than the fluctuations of κ_ℓ . The molecules CN, CH, and C₂, on the other hand, have the opposite temperature dependence of κ_ℓ , and thus the fluctuations of the continuum opacity effectively cancel the fluctuations of the line opacity. The corrections

$\Delta_{3D-(3D)}$ for CN, CH, and C₂ are therefore much smaller in the near-IR than in the red.

3.5. Abundance corrections at 2.5 μm

As a test case, we also calculated the $3D$ – $1D$ corrections for several fictitious lines of different neutral, ionized atoms and molecules at 2.5 μm (not shown in Figs. 3–5). In this case the $\Delta_{3D-(3D)}$, $\Delta_{\langle 3D \rangle-1D}$, and Δ_{3D-1D} abundance corrections, as well as their dependence on the line parameters, were very similar to those obtained at 1.6 μm . This result is hardly surprising since opacity in the red giant atmospheres at 1.6 – 2.6 μm is dominated by H⁺ free-free transitions, the efficiency of which varies very little in this wavelength range. Thus, the line formation regions are essentially the same at both wavelengths, which leads to very similar line formation properties and $3D$ – $1D$ abundance corrections.

3.6. Line formation in the 1D model atmospheres: influence of the mixing-length parameter α_{MLT}

According to the classical Schwarzschild criterion, 1D LHD models of the red giant studied here are convectively stable in the outer photospheric layers ($\log \tau_{\text{Ross}} \lesssim 1$), irrespective of the mixing length parameter, α_{MLT} (Kučinskas et al. 2005; Ludwig & Kučinskas 2012). Since line formation depths typically never reach deeper than $\log \tau_{\text{Ross}} \approx 0.6$, the choice of α_{MLT} should have no effect on the resulting spectral line strengths. The only exceptions may occur in case of near-infrared lines and/or lines characterized by very high excitation potentials (> 8 eV), i.e. those that form deepest in the photosphere and thus may be sensitive to differences in the temperature profiles computed with different mixing-length parameters.

To verify whether this can actually happen, we ran several test calculations using fictitious Fe I (0, 4 eV), Fe II (0, 4, 8 eV), and O II (0, 10 eV) lines located at 850 nm and 1600 nm. We found that differences between the abundances derived using model atmospheres calculated with different mixing-length parameters ($\alpha_{\text{MLT}} = 1, 2$) were always very small. In fact, they never exceeded 0.02 dex and thus may be safely ignored in most situations related with the abundance work in this particular red giant.

3.7. How to use the 3D abundance corrections

We recall that in this work the $3D$ – $1D$ corrections were calculated for very weak spectral lines. While such corrections provide a convenient way to estimate the importance of 3D hydrodynamical effects in the spectral line formation, abundance corrections for stronger lines may be different because of saturation effects, leading to differences in formation depths and introducing a sensitivity to velocity fields (see Appendix B.3).

The theoretical 3D abundance corrections were derived from the comparison of the equivalent width of the same (artificial) spectral line computed with a 3D model and a 1D model. Since the 3D and the 1D models use the same stellar parameters, atomic data, and numerical methods (as far as possible), the resulting *differential* 3D corrections should be applicable to any 1D model, irrespective of the physical details.

For given stellar parameters (T_{eff} , $\log g$, $[M/H]$) and a given element and ionization stage, the 3D abundance correction depends only on the energy of the lower level of the transition, the wavelength of the line, and in principle also on the mixing-length

³ including the indirect temperature dependence via electron pressure.

parameter used for the 1D model, $\Delta_{3D-1D}(\chi, \lambda, \alpha_{MLT})$, provided that the line is *weak* (on the linear part of the curve-of-growth). In this case, the corrections given in Figs. 3, 4, and 5 can be readily applied to the 1D LTE abundance determinations performed with any standard 1D mixing-length model atmosphere: $A(X_i)_{3D} = A(X_i)_{1D} + \Delta_{3D-1D}$. As shown in Sect. 3.6, the dependence on α_{MLT} is negligible for the present stellar parameters.

In the general case of stronger lines, the 3D corrections depend in addition on the equivalent width of the line, W , and on the microturbulence parameter used for the 1D model, ξ_{mic} , $\Delta_{3D-1D}(\chi, \lambda, W, \xi_{mic}; \alpha_{MLT})$, as illustrated in Fig. B.4 for Fe II, $\chi = 10$ eV. Except for this example, we do not provide the dependence of Δ_{3D-1D} on W and ξ_{mic} in this work. The given corrections for the weak line limit can then only serve as an indication of the line's susceptibility to 3D effects. Figure B.4 suggests that the 3D correction for stronger lines is always more positive than in the weak line limit. The figure also seems to indicate that Δ_{3D-1D} becomes independent of W for strong lines, suggesting that a 'strong line limit' might be a useful quantity. Additional investigations are needed to see whether these properties remain valid in general.

4. Conclusions

We have investigated the influence of thermal convection on the spectral line formation in the atmosphere of a red giant located close to the RGB tip ($T_{eff} = 3660$, $\log g = 1.0$, $[M/H] = 0.0$). To this end, we synthesized a large number of fictitious atomic and molecular lines of astrophysically important tracer elements, using for this purpose the 3D hydrodynamical CO⁵BOLD and classical 1D LHD stellar model atmospheres (both types of models sharing identical atmospheric parameters, opacities, equation of state, and chemical composition). The influence of convection on the line formation was investigated by focusing on the differences between the abundances inferred from a given (weak) spectral line by the requirement of producing a given equivalent width with the 3D and 1D model atmospheres, assuming LTE.

Overall, convection plays a considerable role in the atmosphere of the red giant studied here. There are significant horizontal temperature fluctuations seen at different optical depths in the atmosphere that are caused either by convective up- or downflows (inner atmosphere), convective overshoot, and/or shock wave activity (outer atmosphere). This leads to substantial horizontal variations in the number densities of certain chemical species, causing significant deviations from the predictions of a classical 1D model.

Spectral line formation is more or less strongly affected by convection in this particular red giant, depending on the line parameters and the chemical species under consideration. The differences in elemental abundances inferred from a given spectral line with the 3D and 1D model atmospheres, Δ_{3D-1D} , are most pronounced for high-excitation lines of ions and atoms of predominantly neutral elements. Their abundance corrections grow larger with increasing excitation potential, reaching values of $\Delta_{3D-1D} \sim -0.4$ dex for excitation potential $\chi = 10$ eV. The main physical reason for this 3D–1D difference is the increasingly nonlinear temperature dependence of the line opacity as χ increases. In a 3D atmosphere, the horizontal temperature fluctuations then lead to an enhancement of the effective line opacity with respect to the 1D case.

Lines of neutral atoms of predominantly ionized elements show significantly smaller corrections, with Δ_{3D-1D} not exceeding ± 0.1 dex. Here the temperature dependence of the line opacity due to ionization and excitation tend to cancel partially.

Molecular lines show a more complex behavior due to the strong coupling between the different dissociation equilibria. CO is least susceptible to 3D effects, with $|\Delta_{3D-1D}| < 0.03$ dex. NH and OH represent a different category of molecules; their abundance corrections fall in the range $|\Delta_{3D-1D}| < 0.1$ dex. The largest corrections are found for C₂, reaching as low as $\Delta_{3D-1D} \approx -0.16$ dex.

It is important to emphasize that the 3D–1D corrections for all chemical species studied here show a significant wavelength dependence. In most cases, the abundance corrections are significantly smaller in the near-infrared at λ 1600 nm than in the optical spectral range. Careful investigation reveals that this does *not* indicate that the atmospheric layers where the infrared lines originate are least affected by convection. Rather, the strong wavelength dependence of the 3D corrections is related to the fact that the continuum opacity is much more temperature dependent around λ 1600 nm (mainly H⁺ free-free absorption) than around λ 850 nm (mainly H⁺ bound-free absorption). It should be stressed though that this conclusion was reached for the particular red giant studied here and may change with the atmospheric parameters of the star under investigation.

One may thus conclude that the spectral line formation in a red giant photosphere is a delicate process, governed by the subtle interplay between microscopic (atomic line parameters) and macroscopic (local temperature fluctuations) physics. The size of the 3D-hydrodynamical fluctuations and their effects on the line formation process can only be assessed by dedicated radiation hydrodynamics simulations and detailed 3D line formation calculations. For the present example, we find substantial 3D abundance corrections, especially for ionized atoms, suggesting that even at solar metallicity, the accuracy of 1D LTE stellar abundance work can be significantly improved by exploiting the additional information provided by realistic 3D model atmospheres.

Acknowledgements. We thank the referee R. Collet for a comprehensive and constructive report, which helped to improve the paper. This work was supported by grant from the Research Council of Lithuania (MIP-101/2011). HGL acknowledges financial support from EU contract MEXT-CT-2004-014265 (CIFIST), and by the Sonderforschungsbereich SFB 881 "The Milky Way System" (subproject A4) of the German Research Foundation (DFG). AK and HGL acknowledge financial support from the Sonderforschungsbereich SFB 881 "The Milky Way System" (subproject A4) of the German Research Foundation (DFG) that allowed exchange visits between Vilnius and Heidelberg. PB and AK acknowledge support from the Scientific Council of the Observatoire de Paris and the Research Council of Lithuania (MOR-48/2011) that allowed exchange visits between Paris and Vilnius. MS acknowledges funding from the Research Council of Lithuania for a research visit to Vilnius.

References

- Bessell, M., Christlieb, N., Gustafsson, B. 2004, *ApJ*, 612, 61
- Caffau, E., Ludwig, H.-G., Steffen, M., Ayres, T.R., Bonifacio, P., Cayrel, R., Freytag, B., & Plez, B. 2008, *A&A*, 488, 1031
- Caffau, E., Ludwig, H.-G., Steffen, M., Freytag, B., and Bonifacio, P. 2011, *SoPh*, 268, 255
- Collet, R., Asplund, M., & Trampedach, R. 2007, *A&A*, 469, 687
- Cox, A.N. 2000, *Allen's Astrophysical Quantities*, 4th ed.
- Dobrovolskas, V., Kučinskas, A., Ludwig, H.-G., Caffau, E., Klevas, J., & Prakapavičius, D. 2010, *Proc. of 11th Symposium on Nuclei in the Cosmos*, *Proceedings of Science*, ID 288 (arXiv:1010.2507)
- Freytag, B., Steffen, M., Ludwig, H.-G., Wedemeyer-Bhm, S., Schaffnerberger, W., & Steiner, O. 2012, *J. Comp. Phys.*, 231, 919
- Gratton, R. 1985, *A&A*, 148, 105
- Gray, D. F. 2005, *The Observation and Analysis of Stellar Photospheres*, 3rd Edition, Cambridge University Press
- Grevesse, N., & Sauval, A.J. 1998, *Space Sci. Rev.*, 85, 161
- Gustafsson, B., Edvardsson, B., Eriksson, K., Jørgensen, U.G., Nordlund, Å., & Plez, B. 2008, *A&A*, 486, 951

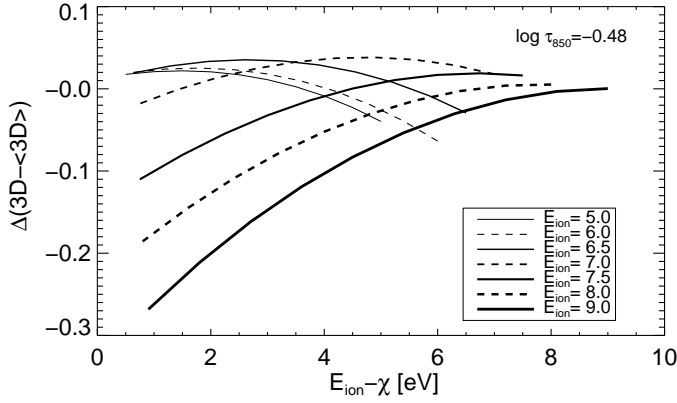


Fig. A.1. Abundance correction $\Delta_{3D-\langle 3D \rangle}$, computed according to Eqs. (A.1) – (A.4), versus the difference between ionization and excitation potential, $E_{\text{ion}} - \chi$. Each curve corresponds to a different value of E_{ion} . The thermodynamic variables $\theta(x, y)$ and $p_e(x, y)$ were taken from the 3D model at monochromatic optical depth $\log \tau_{850} = -0.48$, where the mean temperature is 3360 ± 140 K. The temperature dependence of the partition functions U_0 and U_1 has been neglected.

- Ivanauskas, A., Kučinskas, A., Ludwig, H.-G., & Caffau, E. 2010, Proc. of 11th Symposium on Nuclei in the Cosmos, Proceedings of Science, ID 290 (arXiv: 1010.1722)
- Kučinskas, A., Hauschildt, P.H., Ludwig, H.-G., Brott, I., Vansevičius, V., Lindegren, L., Tanabé, T., & Allard, F. 2005, A&A, 442, 281
- Lambert, D. 1968, MNRAS, 138, 143
- Ludwig, H.-G. 1992, Ph.D. Thesis, Univ. Kiel
- Ludwig, H.-G. & Kučinskas, A. 2012, A&A, in press
- Ludwig, H.-G., Jordan, S., & Steffen, M. 1994, A&A, 284, 105
- Ludwig, H.-G., Caffau, E., Steffen, M., Freytag, B., Bonifacio, P., & Kučinskas, A. 2009, Mem. Soc. Astron. Italiana, 80, 711
- Magain, P. 1986, A&A, 163, 135
- Mihalas, D. 1978, Stellar Atmospheres, Freeman and Company
- Nordlund, Å. 1982, A&A, 107, 1
- Spite, M., Cayrel, R., Plez, B., Hill, V., Spite, F., Depagne, E., François, B., Bonifacio, P., Barbey, B., Beers, T., Andersen, J., Molaro, P., Nordström, B., and Primas, F. 2005, A&A, 430, 655
- Steffen, M. and Holweger, H. 2002, A&A, 387, 258
- Steffen, M., Ludwig, H.-G., & Freytag, B. 1995, A&A, 300, 473
- Vögler, A., Bruls, J.H.M.J., & Schüssler, M. 2004, A&A, 421, 741

Appendix A: Analysis of the abundance corrections for lines of neutral atoms

The temperature sensitivity of spectral lines originating from the neutral atoms of partially ionized species (e.g. Mg I, Ca I, Fe I) is governed by the Saha and Boltzmann equations, i.e. by changes of the degree of ionization and of the excitation of the line's lower level. In the following, we develop a simplified model of the 3D–⟨3D⟩ abundance corrections, which result from horizontal fluctuations of the thermodynamical quantities.

The ratio of the total number of neutral atoms n_0 (with ionization energy E_{ion} and partition function U_0) to the total number of singly ionized atoms n_1 (with partition function U_1) at temperature $T = 5040/\theta$ and electron pressure p_e is given by Saha's equation (see e.g. Gray 2005, Eq. 1.20)

$$\begin{aligned} \log \frac{n_0}{n_1} &= E_{\text{ion}} \theta + 2.5 \log \theta + \log p_e + \log \frac{U_0(\theta)}{U_1(\theta)} - 9.08 \\ &\equiv \log f(\theta, p_e). \end{aligned} \quad (\text{A.1})$$

The opacity of a line transition with lower level excitation potential χ is proportional to the number of absorbing atoms (per unit mass) in this state of excitation,

$$\kappa_\ell \sim \frac{n_0}{n_0 + n_1} 10^{-\theta\chi} = \frac{1}{1 + f^{-1}(\theta, p_e)} 10^{-\theta\chi}. \quad (\text{A.2})$$

In the presence of horizontal fluctuations of θ and p_e , the average line opacity is amplified with respect to the ⟨3D⟩ case by a factor

$$\mathcal{A}_\ell(\tau_c) = \frac{\langle \kappa_\ell(\theta, p_e) \rangle_{x,y}}{\kappa_\ell(\langle \theta \rangle_{x,y}, \langle p_e \rangle_{x,y})}, \quad (\text{A.3})$$

where $\langle \cdot \rangle_{x,y}$ denotes horizontal averaging at constant continuum optical depth τ_c . Assuming that fluctuations of the continuum opacity and the source function can be neglected, the abundance correction for weak lines can be estimated as

$$\Delta_{3D-\langle 3D \rangle} \approx -\log \mathcal{A}_\ell. \quad (\text{A.4})$$

Figure A.1 shows the result of computing $\Delta_{3D-\langle 3D \rangle}$ according to Eqs. (A.1) – (A.4) for different combinations of χ and E_{ion} . The figure illustrates how the curves $\Delta_{3D-\langle 3D \rangle}$ versus $E_{\text{ion}} - \chi$ change systematically as the parameter E_{ion} increases from 0 to 9 eV. For $E_{\text{ion}} \lesssim 6$ eV, the neutral atoms are a minority species, $f \ll 1$, and we see from Eq. (A.2) that in this case

$$\kappa_\ell \sim f 10^{-\theta\chi} \sim 10^{\theta(E_{\text{ion}} - \chi)} \quad (\text{A.5})$$

depends only on the difference $(E_{\text{ion}} - \chi)$, such that all curves with $E_{\text{ion}} \lesssim 6$ eV fall on top of each other. As E_{ion} increases further, the vertex of the curves moves from $(E_{\text{ion}} - \chi)_{\text{max}} = 0$ eV to ≈ 4 eV to 9 eV as the ionization balance shifts from $\langle f \rangle_{x,y} \approx 0$ ($E_{\text{ion}} = 0$ eV) to ≈ 1 ($E_{\text{ion}} = 7$ eV) to ≈ 1000 ($E_{\text{ion}} = 9$ eV). In fact, it can be shown analytically that

$$(E_{\text{ion}} - \chi)_{\text{max}} \approx E_{\text{ion}} \frac{\langle f \rangle_{x,y}}{1 + \langle f \rangle_{x,y}}. \quad (\text{A.6})$$

Admittedly, the description of the abundance corrections developed above is severely simplified. It ignores the fact that the line formation region is extended and that the location of its center of gravity depends sensitively on E_{ion} and χ (cf. Figs. A.2, B.1, C.2). Also, fluctuations of the continuum opacity and the source function were neglected. Nevertheless, the systematics seen in Fig. A.1 provides a basic explanation of the detailed numerical results presented in Sect. 3.2, Fig. 3 (especially middle left panel).

Appendix B: Analysis of the abundance corrections for high-excitation lines of ions

In the following, we analyze in some detail the abundance corrections derived for the high-excitation Fe II lines, which are representative of the ionized atoms and show the largest 3D corrections (see Fig. 4). Evaluating the *equivalent width contribution functions* of this line in the 3D and the 1D models, we determine the physical cause of the abundance corrections. In particular, we can understand the sign of the 3D–⟨3D⟩ and ⟨3D⟩–1D corrections and explain why these corrections are so much smaller at λ 1600 nm than at λ 850 nm.

For simplicity, we consider only vertical rays (disk-center intensity) in a single snapshot from the 3D simulation, noting that the qualitative behavior of the abundance corrections is similar for intensity and flux, and does not vary much in time, i.e. the 3D–⟨3D⟩ correction is always strongly negative, while the ⟨3D⟩–1D correction is slightly positive at λ 850 nm.

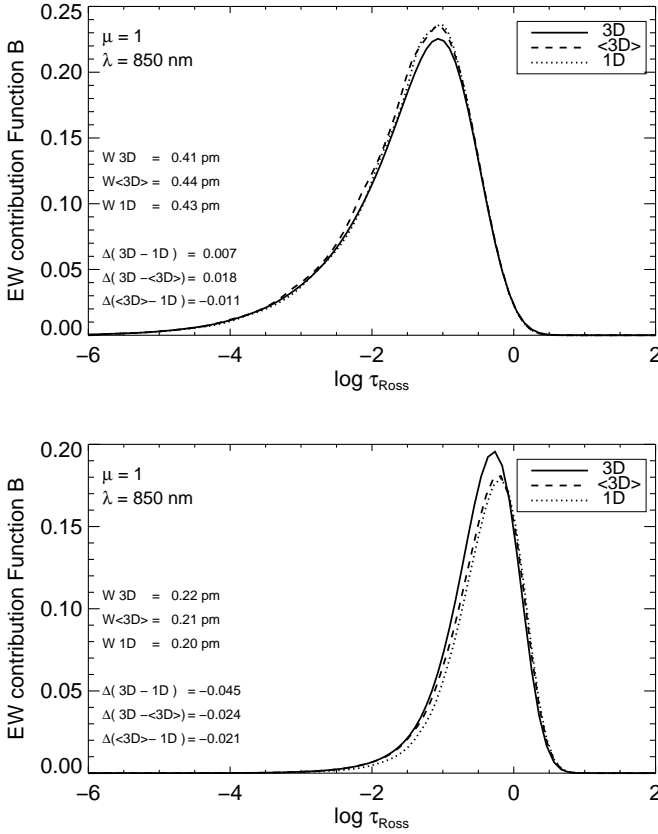


Fig. A.2. Disk-center ($\mu = 1$) equivalent width contribution functions, $\mathcal{B}(\log \tau_c)$, of a weak (artificial) Fe I line with excitation potential $\chi = 0$ eV (top) and $\chi = 5$ eV (bottom), at wavelengths λ 850 nm, evaluated according to the weak line approximation (Eqs. B.5, B.7), for a single snapshot of the 3D model, the corresponding $\langle 3D \rangle$ average model, and the associated 1D LHD model used in this work. The contribution functions, originally defined on the monochromatic optical depth scale, have been transformed to the Rosseland optical depth scale.

B.1. Formalism

Following Magain (1986), the *line depression contribution function* (for vertical rays, LTE), C_I^D , is defined in Linfor3D as

$$C_I^D(\Delta\lambda, \tau_c) = \langle \eta(\Delta\lambda, \tau_c) u_c(\tau_c) \exp\{-(\tau_c + \tau_\ell(\Delta\lambda, \tau_c))\} \rangle_{x,y} \quad (\text{B.1})$$

where τ_c is the continuum optical depth, $\eta(\Delta\lambda, \tau_c) = \kappa_\ell(\Delta\lambda, \tau_c)/\kappa_c(\tau_c)$ is the ratio of line opacity to continuum opacity, $u_c(\tau_c) = I_c^+(\tau_c) - S_c(\tau_c)$ is the difference between outgoing continuum intensity and source function⁴, and $(\tau_c + \tau_\ell(\Delta\lambda))$ is the total optical depth in the line; angle brackets $\langle \cdot \rangle_{x,y}$ indicate horizontal averaging at constant continuum optical depth. Note that η (and τ_ℓ) vary with wavelength position in the line profile, $\Delta\lambda$, whereas τ_c and u_c can be considered as constant across the line profile. Then the absolute line depression at any wavelength in the line profile is

$$D_I(\tau_c = 0, \Delta\lambda) = \int_0^\infty C_I^D(\Delta\lambda, \tau'_c) d\tau'_c. \quad (\text{B.2})$$

⁴ u_c is also called ‘source function gradient’ since $u_c = dS_c/d\tau_c$ in the diffusion approximation, and if S_c is a linear function of τ_c .

Defining further the *equivalent width contribution function* as

$$C_I^W(\tau_c) = \int_{-\infty}^{+\infty} C_I^D(\Delta\lambda', \tau_c) d\Delta\lambda', \quad (\text{B.3})$$

the equivalent width of the line is finally computed as

$$\begin{aligned} W_I &= \frac{1}{\langle I_c \rangle} \int_0^\infty C_I^W(\tau'_c) d\tau'_c \\ &= \frac{1}{\langle I_c \rangle} \int_{-\infty}^\infty \mathcal{B}(\log \tau'_c) d \log \tau'_c, \end{aligned} \quad (\text{B.4})$$

where $\langle I_c \rangle$ is the horizontally averaged emergent continuum intensity, and \mathcal{B} is defined as

$$\mathcal{B}(\tau_c) = \ln 10 \tau_c C_I^W(\tau_c). \quad (\text{B.5})$$

In the limit of *weak lines*, we can assume that $\tau_\ell \ll \tau_c$ over the whole line formation region, and Eqs. (B.1) and (B.3) simplify to

$$C_I^D(\Delta\lambda, \tau_c) = \exp\{-\tau_c\} \langle \eta(\Delta\lambda, \tau_c) u_c(\tau_c) \rangle_{x,y}, \quad (\text{B.6})$$

and

$$C_I^W(\tau_c) = \exp\{-\tau_c\} \langle \eta_0(\tau_c) u_c(\tau_c) \rangle_{x,y}, \quad (\text{B.7})$$

where

$$\eta_0(\tau_c) = \int_{-\infty}^{+\infty} \eta(\Delta\lambda', \tau_c) d\Delta\lambda'. \quad (\text{B.8})$$

In this weak line limit, C_I^D , and hence C_I^W are strictly proportional to the line opacity, and the equivalent width scales linearly with the *gf*-value of the line (or the respective chemical abundance). Then the 3D abundance corrections can simply be obtained from the equivalent widths as

$$\begin{aligned} \Delta_{3D-1D} &= -\log(W_{3D}/W_{1D}), \\ \Delta_{3D-\langle 3D \rangle} &= -\log(W_{3D}/W_{\langle 3D \rangle}), \\ \Delta_{\langle 3D \rangle-1D} &= -\log(W_{\langle 3D \rangle}/W_{1D}). \end{aligned} \quad (\text{B.9})$$

B.2. Analysis of mixed contribution functions

Figure B.1 compares the equivalent width contribution functions, \mathcal{B} , of a weak (artificial) Fe II line with excitation potential $\chi = 10$ eV at two wavelengths, λ 850 nm (top) and λ 1600 nm (bottom), for the 3D model, the corresponding $\langle 3D \rangle$ average model, and the associated 1D LHD model used in this work. For each of the different models the area below the corresponding curve is proportional to the equivalent width of the emerging line profile. At λ 850 nm, the equivalent width produced by the 3D model is significantly larger than that of the 1D LHD model, which in turn is significantly larger than that of the $\langle 3D \rangle$ model, assuming the same iron abundance in all cases. The abundance corrections derived with Eq. (B.9) are $\Delta_{3D-1D} = -0.33$, $\Delta_{3D-\langle 3D \rangle} = -0.46$, and $\Delta_{\langle 3D \rangle-1D} = +0.13$ dex. These numbers are fully consistent with the results shown in Fig. 4. At λ 1600 nm, on the other hand, the equivalent widths obtained from the three different model atmospheres are obviously very similar; all abundance corrections are much smaller than those at λ 850 nm, again in basic agreement with the results shown in Fig. 4.

Figure B.1 also shows that the formation region of this high-excitation Fe II line is well confined to a narrow region in the deep photosphere, mainly below $\tau_{\text{Ross}} = 1$, where the degree of ionization of iron is changing rapidly with depth. As expected,

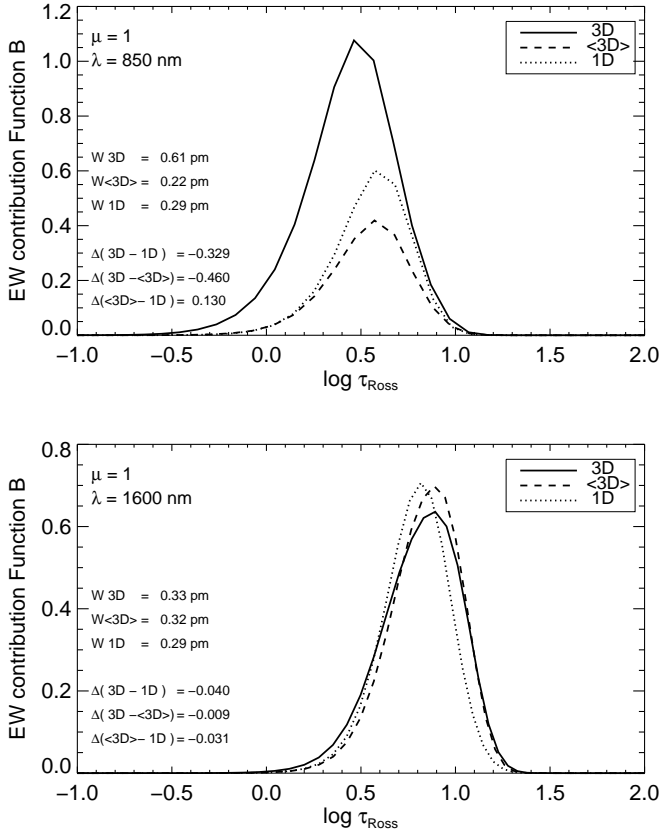


Fig. B.1. Disk-center ($\mu = 1$) equivalent width contribution functions, $\mathcal{B}(\log \tau_c)$, of a weak (artificial) Fe II line with excitation potential $\chi = 10$ eV, at wavelengths λ 850 nm (top) and λ 1600 nm (bottom), evaluated according to the weak line approximation (Eqs. B.5, B.7), for a single snapshot of the 3D model, the corresponding <3D> average model, and the associated 1D LHD model used in this work. The contribution functions, originally defined on the monochromatic optical depth scale, have been transformed to the Rosseland optical depth scale as a common reference.

the line originates from somewhat deeper layers at λ 1600 nm (minimum of H^- opacity) than at λ 850 nm (maximum of H^- opacity). According to Fig. 1, both the amplitude of the horizontal temperature fluctuations and the 1D - <3D> temperature difference increase with depth in the range $-1 < \log \tau_{\text{Ross}} < +1$, such that they are larger in the line formation region at λ 1600 nm. Naively, one would thus expect the amplitude of the abundance corrections $\Delta_{3D-\langle 3D \rangle}$ and $\Delta_{\langle 3D \rangle-1D}$ to be *larger* at λ 1600 nm than at λ 850 nm. However, this reasoning obviously fails. As we have seen before, the abundance corrections are found to be strikingly *smaller* at λ 1600 nm. Additional analysis is necessary to resolve this apparent contradiction.

To understand the origin of the abundance corrections, we need to understand the role of the different factors that make up the contribution function \mathcal{B} , essentially u_c and $\eta_0 = \kappa_\ell / \kappa_c$. The different behavior of these factors in the different types of models determines the sign and amplitude of the abundance corrections. In the following, subscripts 1, 2, and 3 refer to the 1D LHD

Table B.1. Abundance corrections for the Fe II line ($\chi = 10$ eV) derived from mixed contribution functions $\mathcal{B}_{i,j,k}$ at λ 850 and 1600 nm.

Case	$i j k m$	$\Delta_{i,j,k,m}$ 850 nm	$\Delta_{i,j,k,m}$ 1600 nm	$i j k m$	$\Delta_{i,j,k,m}$ 850 nm	$\Delta_{i,j,k,m}$ 1600 nm
0	2 2 2 2	0.000	0.000	1 1 1 1	0.000	0.000
1	3 2 2 2	0.014	0.036	2 1 1 1	0.062	-0.053
2	2 3 2 2	-0.451	-0.146	1 2 1 1	0.140	0.150
3	3 3 2 2	-0.558	-0.165	2 2 1 1	0.202	0.093
4	2 2 3 2	0.003	-0.132	1 1 2 1	-0.077	-0.130
5	3 2 3 2	0.046	-0.040	2 1 2 1	-0.015	-0.184
6	2 3 3 2	-0.374	-0.015	1 2 2 1	0.069	0.026
7	3 3 3 2	-0.460	-0.009	2 2 2 1	0.130	-0.031

model, the <3D> model, and the 3D model, respectively. With this notation in mind, we define the *mixed contribution functions*

$$\mathcal{B}_{i,j,k}(\tau_c) = \ln 10 \tau_c \exp\{-\tau_c\} \left\langle u_{c,i}(\tau_c) \frac{\kappa_{\ell,j}(\tau_c)}{\kappa_{c,k}(\tau_c)} \right\rangle_{x,y}, \quad (\text{B.10})$$

where $i = 1 \dots 3$, $j = 1 \dots 3$, $k = 1 \dots 3$. The three mixed contribution functions with three identical subscripts $i = j = k$ are thus the *normal* contribution functions for the 1D, <3D>, and 3D model, respectively. From each of the $\mathcal{B}_{i,j,k}$ we can compute an equivalent width according to Eq. (B.4), which we denote as $W_{i,j,k}$. The equivalent widths can then be used to derive abundance corrections via

$$\Delta_{i,j,k,m} = -\log(W_{i,j,k}/W_{m,m,m}). \quad (\text{B.11})$$

The numerical evaluation of the relevant abundance corrections is compiled in Table B.2.

B.2.1. <3D>–1D abundance corrections

With the help of Table B.2, the physical interpretation of the $\Delta_{\langle 3D \rangle-1D}$ abundance correction is straightforward. Columns (6) and (7) show the effect of the different factors that contribute to the <3D>–1D abundance correction. Owing to the different thermal structure of the two model atmospheres, all three factors, u_c , κ_ℓ , and κ_c change simultaneously, and the full correction is $\Delta_{\langle 3D \rangle-1D} = \Delta_{2,2,2,1}$, listed in the last row of the Table as case (7). The other cases (1)–(6) refer to ‘experiments’ where only one or two of the factors are allowed to change while the remaining factors are fixed to expose the abundance corrections due to the individual factors. Case (1), for example, shows the correction that would result for fixed opacities, $\kappa_\ell(\tau_c)$, $\kappa_c(\tau_c)$, accounting only for the differences in the source function gradient u_c . Case (6) shows the complementary experiment where u_c is fixed and both opacities are changing in accordance with the different thermodynamical conditions.

At λ 850 nm, the continuum opacity is dominated by H^- bound-free absorption, which shows its maximum at this wavelength. The high-excitation Fe II line forms around $\log \tau_{850} \approx +0.7$ ($\log \tau_{\text{Ross}} \approx +0.6$), i.e. significantly below continuum optical depth unity. At this depth, both the temperature and the temperature gradient are slightly lower in the <3D> model than in the 1D model. As a consequence, both u_c and κ_c decrease toward the <3D> model, approximately by the same factor (see cases 1 and 4), and hence their effects cancel out. The highly temperature-dependent line opacity ($\partial \log \kappa_\ell / \partial \theta \approx -10$; $\theta = 5040/T$) is thus

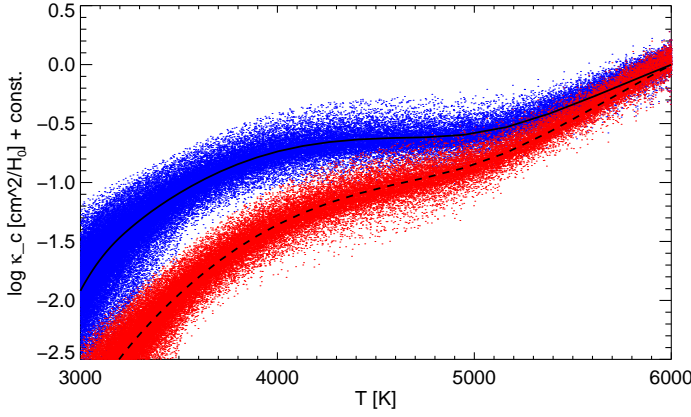


Fig. B.2. Continuous opacity due to H_{bf}^- at λ 850 nm (solid line, cloud of blue dots), and due to H_{ff}^- at λ 1600 nm (dashed line, cloud of red dots), as a function of temperature in the 3D model (dots) and in the $\langle 3D \rangle$ model (lines), respectively. The opacities have been computed according to Eqs. (8.12) and (8.13) by Gray (2005); they are given in units of cm^2 per neutral hydrogen atom, and have been normalized to 1 at $T = 6000$ K. Both opacities are proportional to the electron pressure, and their ratio is a simple monotonic function of temperature. Note that $\kappa(H_{\text{bf}}^-)$ is almost temperature insensitive between $T = 4000$ and 5000 K.

the dominating factor and determines the total $\Delta_{(3D)-(1D)}$ abundance correction (compare cases 2 and 7).

At λ 1600 nm, the situation is different. Here the continuum opacity is mainly due to H^- free-free absorption. The important difference is that the temperature sensitivity of the H^- free-free opacity is significantly higher than that of the H^- bound-free absorption (see Fig. B.2). In the line formation region around $\log \tau_{1600} \approx +0.15$ ($\log \tau_{\text{Ross}} \approx +0.85$), the temperature sensitivity of κ_ℓ and κ_c is now comparable, such that the ratio of both opacities is nearly the same in the two models. The corrections due to κ_ℓ and κ_c are almost equal and of opposite sign (cases 2 and 4), and hence cancel out. At the same time, the source function gradient is very similar in both models, and thus the correction due to u_c is small (case 1). The total $\Delta_{(3D)-(1D)}$ abundance correction is therefore significantly smaller than at λ 850 nm (case 7).

B.2.2. 3D– $\langle 3D \rangle$ abundance corrections

The physical interpretation of the $\Delta_{3D-(3D)}$ abundance correction proceeds along similar lines. Columns (3) and (4) of Table B.2 show the influence of the different factors that contribute to the 3D– $\langle 3D \rangle$ ‘granulation correction’. The three factors, u_c , κ_ℓ , and κ_c differ between the 3D and the $\langle 3D \rangle$ model due to the presence of horizontal fluctuations of the thermodynamical conditions at constant optical depth τ_c , which then lead to more or less *non-linear* fluctuations of the factors that make up the contribution function. The full correction, $\Delta_{3D-(3D)} = \Delta_{3,3,3,2}$, allows for fluctuations in all three factors and is listed in the last row of the table as case (7). The other cases (1)–(6) refer to ‘experiments’ where the fluctuations are artificially suppressed for one or two of the factors to study the impact of the fluctuations of the individual factors on the resulting the abundance correction. For example, case (5) shows the correction that would result if the fluctuations of the line opacity, $\kappa_\ell(\tau_c)$, were suppressed. case (2) shows the complementary experiment where only $\kappa_\ell(\tau_c)$ is allowed to fluctuate, while u_c and κ_c are fixed.

At λ 850 nm, our weak Fe II line is strongly enhanced in the 3D model due to the nonlinear fluctuations of the line opacity. The fluctuations lead to a line enhancement, and hence to *negative* 3D– $\langle 3D \rangle$ abundance corrections, whenever $\langle \kappa_\ell(T) \rangle_{x,y} > \kappa_\ell(\langle T \rangle_{x,y})$, which happens to be the case as $\kappa_\ell \propto \exp\{-E/kT\}$ (roughly speaking because $\partial^2 \kappa_\ell / \partial T^2 > 0$). As can be deduced from the comparison of cases (2) and (7), suppression of the fluctuations of both u_c and κ_c does not change the resulting 3D abundance correction. We can furthermore see that the fluctuations of u_c enhance the nonlinearity of the fluctuations of κ_ℓ (case 3) and that the fluctuations of κ_c diminish the nonlinearity of the fluctuations of κ_ℓ (case 6). We conclude that the fluctuations of u_c and κ_c must be substantial, but essentially linear, such that they do not produce any significant abundance corrections on their own (cases 1, 4, and 5).

At λ 1600 nm, the continuum opacity κ_c is lower than at λ 850 nm, and our weak Fe II line forms at somewhat deeper layers where the temperature is higher. Equally important, the temperature sensitivity of κ_c is distinctly higher at λ 1600 nm than at λ 850 nm, as is demonstrated in Fig. B.2. This fact is the key to understanding the drastically smaller abundance corrections found at λ 1600 nm.

Comparing the effect of the line opacity fluctuations for the two wavelengths (case 2), we see that the corresponding abundance correction is significantly smaller at λ 1600 nm. This result is unexpected, because according to Fig. 1 the temperature fluctuations, δT_{rms} , ought to be larger in the deeper layers where the near-IR line forms, which in turn should lead to more nonlinear fluctuations of the line opacity and hence larger abundance corrections at λ 1600 nm compared to λ 850 nm.

Further investigations revealed that the opposite is true. The point is that we have to distinguish between fluctuations at constant Rosseland optical depth, τ_{Ross} , and fluctuations at constant monochromatic optical depth, τ_c , which are relevant in the present context. In fact, the higher temperature sensitivity of the continuum opacity at λ 1600 nm *reduces* the amplitude of the temperature fluctuations at constant continuum optical depth τ_{1600} with respect to the fluctuations at constant τ_{850} , as illustrated in Fig. B.3 (top panel). The degree of nonlinearity of the line opacity fluctuations, as measured by the ratio of average line opacity to line opacity at mean temperature, $\mathcal{A}_\ell = \langle \kappa_\ell(T) \rangle / \kappa_\ell(\langle T \rangle)$, is shown in the bottom panel of Fig. B.3. Over the whole depth range, the nonlinearity of the κ_ℓ fluctuations is higher at constant τ_{850} than at constant τ_{1600} . Remarkably, \mathcal{A}_ℓ increases toward lower temperatures, even though the amplitude of the temperature fluctuations decreases with height. This is because the temperature sensitivity of κ_ℓ increases strongly as Fe II becomes a minority species at lower T (cf. Fig. 2). The fact that \mathcal{A}_ℓ is significantly higher for the red line at λ 850 nm than for the near-IR line at λ 1600 nm explains the wavelength dependence of the abundance corrections found for case (2), columns (3) and (4).

Comparing cases (2) and (6) for the near-IR line, we see that the abundance correction essentially vanishes when combining the fluctuations of the line opacity with the fluctuations of the continuum opacity. We note that the fluctuations of κ_c are significantly larger at $\log \tau_{1600} = 0.15$, where the near-IR line forms, than at $\log \tau_{850} = 0.7$, where the red line forms, even though the temperature fluctuations are lower (see Fig. B.3). This is again a consequence of the enhanced temperature sensitivity of the continuum opacity at λ 1600 nm (Fig. B.2). It thus happens that the abundance corrections due to the fluctuations of the continuum opacity and the line opacity, respectively, are comparable (compare cases 2 and 4). The net result is a cancelation of the two

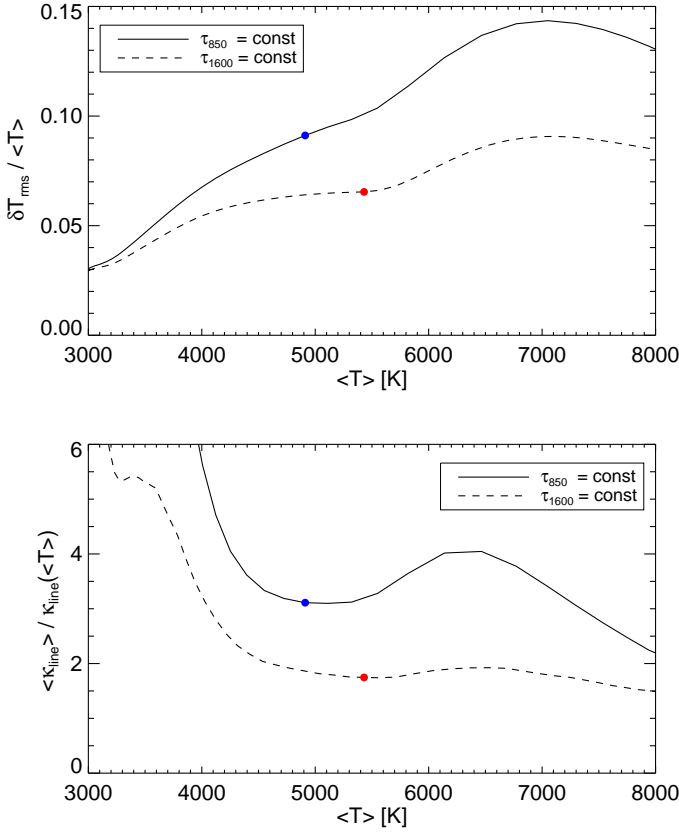


Fig. B.3. Amplitude of the (relative) temperature fluctuations, $\delta T_{\text{rms}} / \langle T \rangle$ (top), and ratio of average line opacity to line opacity at mean temperature, $\mathcal{A}_\ell = \langle \kappa_\ell(T) \rangle / \kappa_\ell(\langle T \rangle)$ of a weak (artificial) Fe II line with excitation potential $\chi = 10$ eV (bottom) as a function of the mean temperature $\langle T \rangle$, where angle brackets indicate horizontal averaging at constant monochromatic optical depth. Solid and dashed curves show the results of averaging on surfaces of constant τ_{850} and constant τ_{1600} , respectively. Filled dots indicate the location of the center of the line formation regions at $\lambda = 8500$ and 1600 nm.

effects. The total $\Delta_{3\text{D}-(3\text{D})}$ abundance correction at $\lambda = 1600$ nm is therefore small.

B.3. Saturation effects

So far we have considered the abundance corrections for the limiting case of weak, unsaturated lines. In this limit, the abundance corrections are independent of the equivalent width of the line and of the microturbulence parameter ξ_{mic} chosen for the spectrum synthesis with the 1D models. Figure B.4 shows how the results change if saturation effects are fully taken into account, again for the example of the high-excitation Fe II line.

Obviously, the total 3D abundance correction, $\Delta_{3\text{D}-1\text{D}}$, depends strongly on both the assumed value of ξ_{mic} and on the line strength, $W_{3\text{D}}$. We notice that this holds even for very weak lines, and conclude that even the weakest lines used for this study are already partly saturated. Plotting $\log W_{3\text{D}}$ versus $\log gf$ reveals that the curve-of-growth is linear, and thus saturation effects can be safely ignored as long as the equivalent width of the line is below $W_{3\text{D}}^* \approx 0.001$ pm at $\lambda = 850$ nm ($W_{3\text{D}}^* \approx 0.1$ pm at $\lambda = 1600$ nm). As soon as this line becomes detectable, it is no longer on the

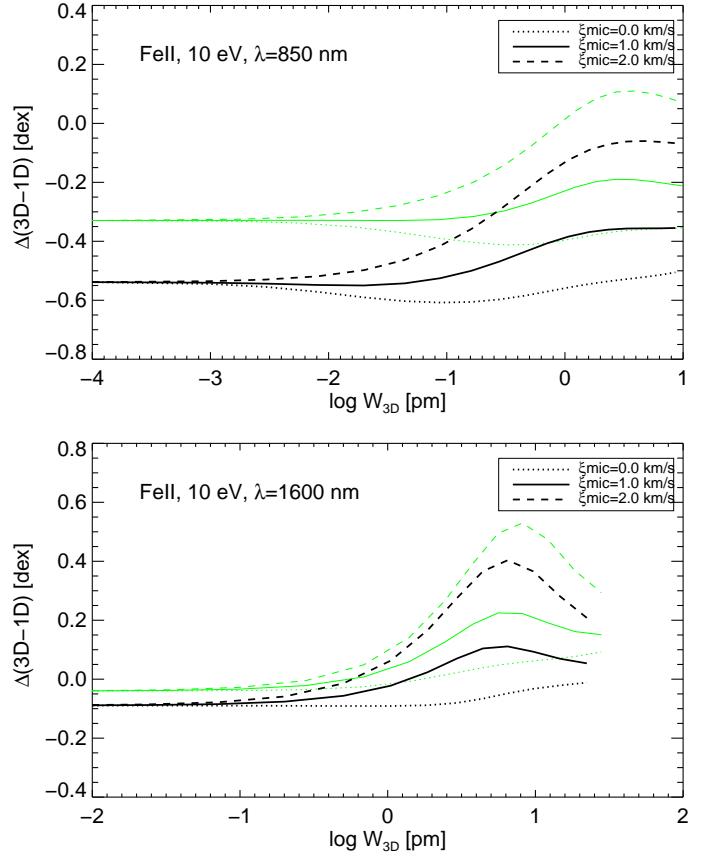


Fig. B.4. Total 3D abundance correction $\Delta_{3\text{D}-1\text{D}}$ for the artificial Fe II line with excitation potential $\chi = 10$ eV at $\lambda = 850$ nm (top) and $\lambda = 1600$ nm (bottom) as a function of the equivalent width obtained from the 3D model. The fainter (green) curves and the thicker (black) curves refer to the intensity ($\mu = 1$) and flux spectrum, respectively. The abundance corrections have been computed for three different values of the microturbulence parameter used with the 1D model, $\xi_{\text{mic}} = 0.0$ (dotted), 1.0 (solid), and 2.0 km/s (dashed lines). The weak line limit coincides with the horizontal part of the curves at low $\log W_{3\text{D}}$.

linear part of the curve-of-growth. This extreme behavior is of course related to the extreme temperature sensitivity of this high-excitation line, which changes the line-to-continuum opacity ratio from $\eta \ll 1$ to $\eta \gg 1$ within the line formation region. This is especially true at $\lambda = 850$ nm, where the continuum opacity is less temperature dependent (see above). The partial saturation of weak lines is not a particular property of the 3D model, but is seen in 1D models, too.

The top panel of Fig. B.5 shows the equivalent width contribution functions $\mathcal{B}(\tau_{\text{Ross}})$ of the same weak Fe II line ($\chi = 10$ eV, $\lambda = 850$ nm) as in Fig. B.1 (top), but now including the saturation factor $\exp\{-\tau_\ell\}$ (see Eq. B.1). Comparison with Fig. B.1 (top) demonstrates that including the saturation factor reduces the equivalent width from $W_{3\text{D}} \approx 0.61$ pm to $W_{3\text{D}} \approx 0.17$ pm. Moreover, all contribution functions are shifted to slightly higher layers because of the presence of saturation effects. The upward shift is more pronounced for the 3D contribution function, because of the strongly nonlinear fluctuations of the saturation factor $\exp\{-\tau_\ell\}$. As a result, $\mathcal{B}(3\text{D})$ now becomes smaller than $\mathcal{B}(\langle 3\text{D} \rangle)$ and $\mathcal{B}(1\text{D})$ in the deepest part of the line-forming region. Therefore, the ratio of 3D to 1D equivalent width becomes smaller than in the weak line limit, where $\mathcal{B}(3\text{D}) > \mathcal{B}(1\text{D})$ over

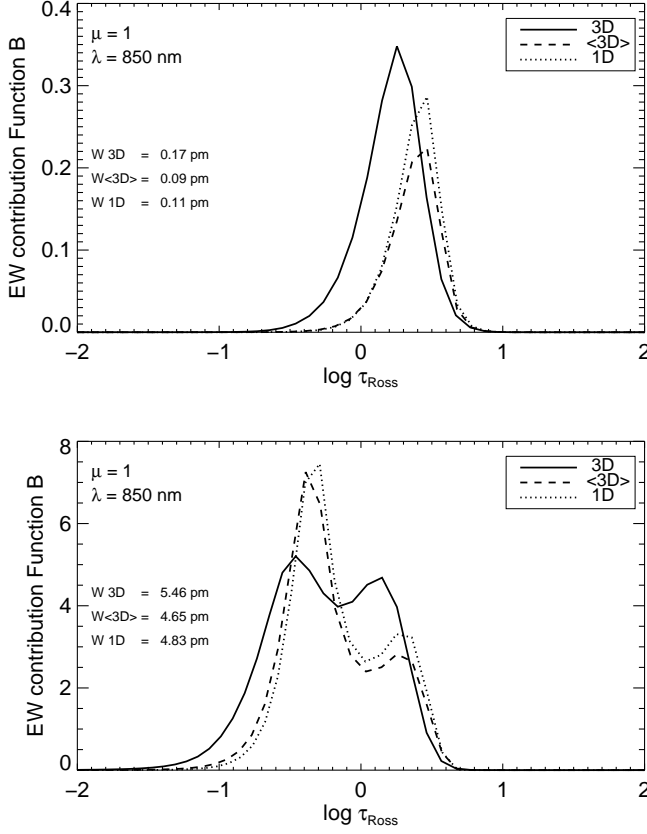


Fig. B.5. Disk-center ($\mu = 1$) equivalent width contribution functions, $\mathcal{B}(\log \tau_c)$, of a weak (top) and strong (bottom) Fe II line with excitation potential $\chi = 10$ eV, at $\lambda 850$ nm. The contribution functions have been computed for a single snapshot of the 3D model (solid), the corresponding (3D) average model (dashed), and the associated 1D LHD model (dotted) used in this work. They have been transformed from the monochromatic to the Rosseland optical depth scale. In all cases, the saturation factor $\exp\{-\tau_\ell\}$ is properly taken into account (see Eq. B.1).

the whole optical depth range. Hence, the total 3D abundance correction, Δ_{3D-1D} , becomes less negative if saturation is taken into account.

If the line strength is increased even more, the contribution functions become wider and extend to higher atmospheric layers, as shown in the bottom panel of Fig. B.5. Recalling that the equivalent width contribution function is a superposition of the line depression contribution functions for the individual wavelength positions in the line profile, it seems evident that the double peak structure is related to the contributions of the line core (left peak) and of the extended line wings (right peak). Test calculations confirm this interpretation. Proceeding from the top to the bottom of the line formation region, the difference $\mathcal{B}(3D) - \mathcal{B}(1D)$ changes sign from positive to negative to positive to negative. Because the contributions of the different layers to the abundance correction cancel partially, a straightforward interpretation of the resulting abundance correction becomes difficult. In principle, a detailed analysis of the line depression contribution functions at individual wavelengths might lead to further insights. Noting, however, that the situation becomes even more complicated when considering flux spectra (involving inclined rays), we have some doubts that such an investigation is worthwhile.

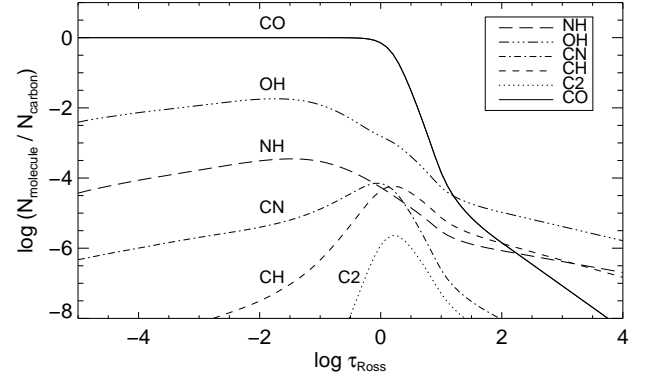


Fig. C.1. Number density of different molecules, normalized to the total number density of carbon (sum over all molecules and ionization states) as a function of the Rosseland optical depth in the 1D LHD model.

Appendix C: Molecule concentrations, line opacities, and height of formation

The equilibrium number density of diatomic molecules with constituents A and B , N_{AB} , is given by the Saha-like relation

$$N_{AB} = Q_{AB}(T) \frac{N_A}{U_A(T)} \frac{N_B}{U_B(T)} \left(\frac{h^2}{2\pi m_{AB} kT} \right)^{3/2} e^{D_0/kT}, \quad (C.1)$$

where N_A and N_B are the number densities (per unit volume) of free neutral atoms (in the ground state) of elements A and B , with partition functions U_A and U_B , respectively; the molecule is characterized by its mass, m_{AB} , its partition function, Q_{AB} , and its dissociation energy D_0 (cf. Cox 2000). Defining the number densities per unit mass as $X_i = N_i/\rho$, where ρ is the mass density, we obtain

$$X_{AB} = \rho Q_{AB}(T) \frac{X_A}{U_A(T)} \frac{X_B}{U_B(T)} \left(\frac{h^2}{2\pi m_{AB} kT} \right)^{3/2} e^{D_0/kT}. \quad (C.2)$$

Figure C.1 shows the number densities of our selection of diatomic molecules (normalized to the total number of carbon nuclei, $N_{AB}/\sum N_C = X_{AB}/\sum X_C$) as a function of Rosseland optical depth in the 1D LHD model used in this work. In the photosphere ($\log \tau_{\text{Ross}} < 0$), essentially all carbon is locked up in CO. The decrease of X_{OH} , X_{NH} , X_{CN} toward lower optical depths is a consequence of the density factor ρ in Eq. (C.2). The destruction of all molecules beyond $\tau_{\text{Ross}} \approx 1$ is due to the Boltzmann factor $\exp\{D_0/kT\}$; a higher dissociation energy corresponds to a steeper drop of the molecule concentration with T .

The opacity of a line with lower transition level energy χ , is proportional to $X_{AB}/Q_{AB} \exp\{-\chi/kT\}$, and thus the line opacity per unit mass can be written as

$$\log \kappa_\ell = \log X_A + \log X_B + \frac{3}{2} \log \theta + (D_0 - \chi) \theta + \log \rho + \text{const.}, \quad (C.3)$$

where $\theta = 5040/T$, and the temperature dependence of the partition functions U_A and U_B has been ignored; the molecular partition function Q_{AB} cancels out.

If both atoms A and B are majority species (e.g. H, N, O for the conditions in our red giant atmosphere), then X_A and X_B are constant, and the temperature dependence of the line opacity is given by

$$\frac{\partial \log \kappa_\ell}{\partial \theta} = D_0 - \chi + \frac{3}{2} \frac{1}{\theta \ln 10} \quad (\rho = \text{const.}) \quad \text{or} \quad (C.4)$$

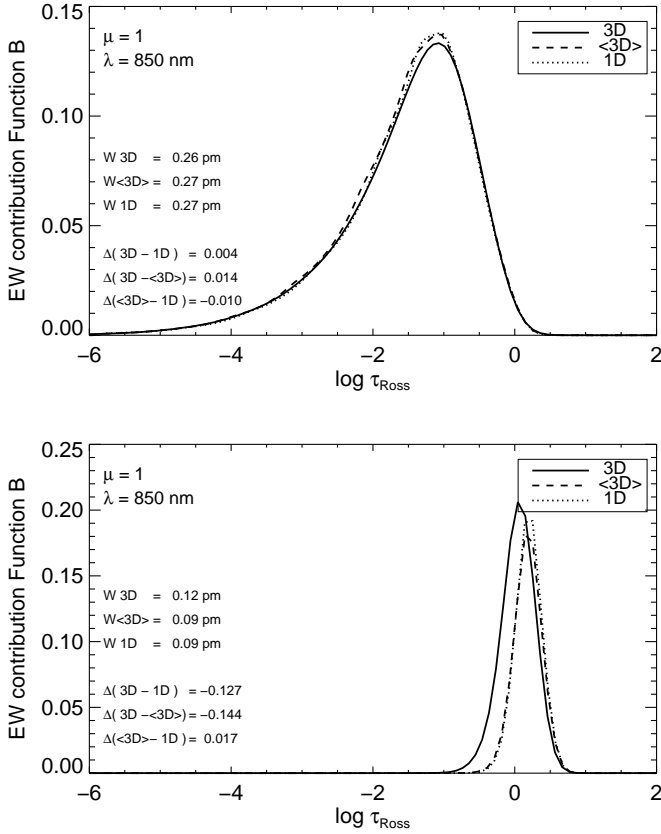


Fig. C.2. Same as Fig. A.2, but for two weak (artificial) molecular lines: a CO line with excitation potential $\chi = 0$ eV (top) and a C_2 line with $\chi = 4$ eV (bottom), both at wavelength λ 850 nm.

$$\frac{\partial \log \kappa_\ell}{\partial \theta} = D_0 - \chi + \frac{5}{2} \frac{1}{\theta \ln 10} \quad (P = \text{const.}). \quad (\text{C.5})$$

In general, the temperature dependence of the molecular line opacity is more complicated, because X_A and/or X_B are more or less strongly temperature dependent due to ionization and/or formation of different molecules. In our red giant atmosphere, for example, the concentration of carbon atoms is controlled by the formation of CO molecules. This leads to a strong *increase* of κ_ℓ with temperature ($\partial \log \kappa_\ell / \partial \theta < 0$) for CH and C_2 at $\tau_{\text{Ross}} < 1$, such that these molecules can only form in a narrow region centered around $\log \tau_{\text{Ross}} \approx 0$ (see Fig. C.2).

Finally, we point out that the molecular lines form in the same height range as the lines of neutral atoms and ions. Figure C.2 displays the contribution functions for the most extreme examples. The ground state CO line (top panel) shows the most extended formation region, centered around $\log \tau_{\text{Ross}} \approx -1$. The contribution function of this line is almost identical to that of the ground state Fe I line shown in Fig. A.2. The high-excitation C_2 line (bottom panel) originates from a very narrow formation region located in the deep photosphere around $\log \tau_{\text{Ross}} \approx 0$. The contribution functions of the other molecular lines considered in this study lie somewhere in between these two extremes; the entire formation region of the molecular lines is always inside the height range covered by our model atmospheres.